Master’s thesis

Master’s Programme in Materials Research
Inorganic Materials Chemistry

Atomic Layer Deposition of $BiVO_4$ for Photocatalysis

Juha Ojala

2022

Supervisors: Mikko Ritala, Markku Leskelä
Examiners: Mikko Ritala, Matti Putkonen

University of Helsinki
Faculty of Science

Tiedekunta – Fakultet – Faculty
Faculty of Science

Koulutusohjelma – Utbildningsprogram – Degree programme
Master’s Programme in Materials Research

Opintosuunta – Studieinrikting – Study track
Inorganic Materials Chemistry

Tekijä – Författare – Author
Juha Ojala

Työn nimi – Arbetets titel – Title
Atomic Layer Deposition of $BiVO_4$ for Photocatalysis

Työn laji – Arbetets art – Level
Master’s Thesis

Aika – Datum – Month and year
September 2022

Sivumäärä – Sidoantal – Number of pages
66

Tiivistelmä – Referat – Abstract

Photocatalysis is a versatile method to use solar energy for chemical processes. Photocatalytic materials absorb light to generate energetic electron-hole pairs that can be used for redox reactions in production of hydrogen and other chemicals, degradation of pollutants, and many other applications. $BiVO_4$ is a visible light absorbing oxide semiconductor with a band gap of about 2.4 eV, and it has received a lot of attention as a standalone photocatalyst and as a photoanode material.

The literature part of this thesis explores how the electronic structure of semiconductors and the different processes in photocatalysis together affect the efficiency of the method. Semiconductor materials are classified based on their chemical composition and compared by selecting most researched materials as examples. Various strategies to improve the photocatalyst material properties are also discussed. Many strategies, such as nanostructured photocatalysts, benefit from deposition of semiconductor thin films. Atomic layer deposition (ALD), as a highly conformal and controllable chemical vapor deposition method, is an excellent choice for depositing semiconductors and various interfacial layers. The literature review also includes a survey of ALD processes for Bi_2O_3 and V_2O_5 and a thorough analysis of the existing $BiVO_4$ ALD processes.

From the selection of binary ALD processes, bismuth(III) 2,3-dimethyl-2-butoxide ($Bi(dmb)_3$), tetrakis(ethylmethylamido)-vanadium(IV) (TEMAV), and water were chosen as precursors to develop a new ALD process for $BiVO_4$. The binary processes were combined in various metal precursor ratios both completely mixed in supercycles and as nanolaminates, and the resulting films were annealed to crystallize the $BiVO_4$. X-ray diffraction was used to characterize the crystalline phases of the films, and it was noticed that TEMAV reacts with Bi_2O_3 to make metallic bismuth, but it is reoxidized by annealing. Composition of the films was investigated with energy dispersive X-ray spectrometry and time-of-flight elastic recoil detection analysis (ToF-ERDA). Some sensitivity to process conditions was observed in the deposition, as the metal stoichiometry varied in unexpected manner between some sets of experiments. ToF-ERDA depth profiles also revealed that mixing of the nanolaminate layers was incomplete with annealing temperatures below 450 °C and with laminate layers over 10 nm in thickness. Scanning electron microscopy was used to study the morphology of the films and revealed a granular, non-continuous structure. The optical properties of the films grown on soda-lime glass were investigated with UV-vis spectrophotometry. The band gaps of the films were estimated to be 2.4–2.5 eV.

The nanolaminate approach to depositing the films was deemed the best, as it avoids most of the reduction of bismuth by TEMAV. However, it is still not clear why this process is so sensitive to process conditions. This should be investigated to further optimize the film stoichiometry. The morphology of the films might be improved by using different substrates, but it is not a critical aspect of the process as there are methods to passivate the exposed substrate surface. Overall, this process has potential to deposit excellent $BiVO_4$ films that are suitable for further research pertaining their photocatalytic properties and modifications such as nanostructured or doped photoanodes.

Avainsanat – Nyckelord – Keywords
Bismuth vanadate, $BiVO_4$, Photocatalysis, Semiconductors, Atomic Layer Deposition

Säilytyspaikka – Förvaringställe – Where deposited
Helda / E-thesis

Muita tietoja – Övriga uppgifter – Additional information

Table of Contents

1 Introduction

Photocatalysis is a light activated chemical process that is mediated by a photocatalyst. The photocatalyst absorbs light and uses the resulting chemical potential energy to initiate reactions that otherwise would not be activated by light alone. This intermediate step differentiates the process from photoactivated chemistry where precursors themselves absorb the light. Photocatalysts come in many different forms ranging from organic dyes and metalorganic complexes[1] to inorganic semiconductors[2] and combinations of these. The focus of this work is on semiconductors and specifically on $BiVO_4$.

There are many types of photocatalysts, and the chemical reactions and applications enabled by them are equally diverse. The so called “holy grail” of photocatalysis is splitting of water into H_2 and O_2 gases for fuel and industrial uses, but many other applications have also been investigated and even commercialized. These include degradation of harmful pollutants in industrial wastewater,[3] self-cleaning windows with photocatalytic coatings,[4] and synthesis of valuable chemicals with selective redox photocatalysts,[5] just to name a few. The greatest advantages of this method are (1) that no inherent photoactivity is required from the precursors and (2) that the solar energy is used directly for the application and hence there is no need for intermediate energy storage or separate equipment for harvesting the energy and utilizing it.

Although photocatalytic water splitting has great potential to reduce dependency on fossil fuels, the efficiency of most photocatalysts is still too low to be viable in practice.[6] Current research aims to change this by creating new materials, modifying existing ones, and exploiting nanoscale and surface effects. One of the main ways to improve photocatalytic systems is to use narrow band gap semiconductors that can also absorb in the visible wavelength range. In this regard $BiVO_4$, with a band gap of about 2.5 eV,[7] has garnered much attention.

In many cases materials can be more efficient in thin film form, because in thin films the photogenerated charge carriers need to travel a shorter distance to reach the surface. Thin film techniques also make heterojunctions and other modifications more efficient in terms of material usage. Physical properties of materials, such as the band gap energy, can also be altered by taking the device dimensions to the nanoscale.[8] Depositing ultra-thin films of a photocatalyst material on the surface of the same photocatalyst can also alter the photocatalytic activity.[9]

One method for making thin films is atomic layer deposition (ALD). It is a chemical vapor deposition technique based on delivering consecutive pulses of highly reactive precursors, which react in a self-limiting fashion with the surface left by the previous precursor.[10] A basic two precursor ALD process is depicted in Figure 1. To prevent unwanted reactions in the gas phase, precursor pulses are separated by purging with inert gas after every pulse. The sequence of pulsing and purging every precursor consecutively is known as an ALD cycle and it is the basis of an ALD process. One cycle deposits a known amount of material (described by growth per cycle, GPC), and the thickness of the deposited film can be digitally controlled by adjusting the number of cycles.

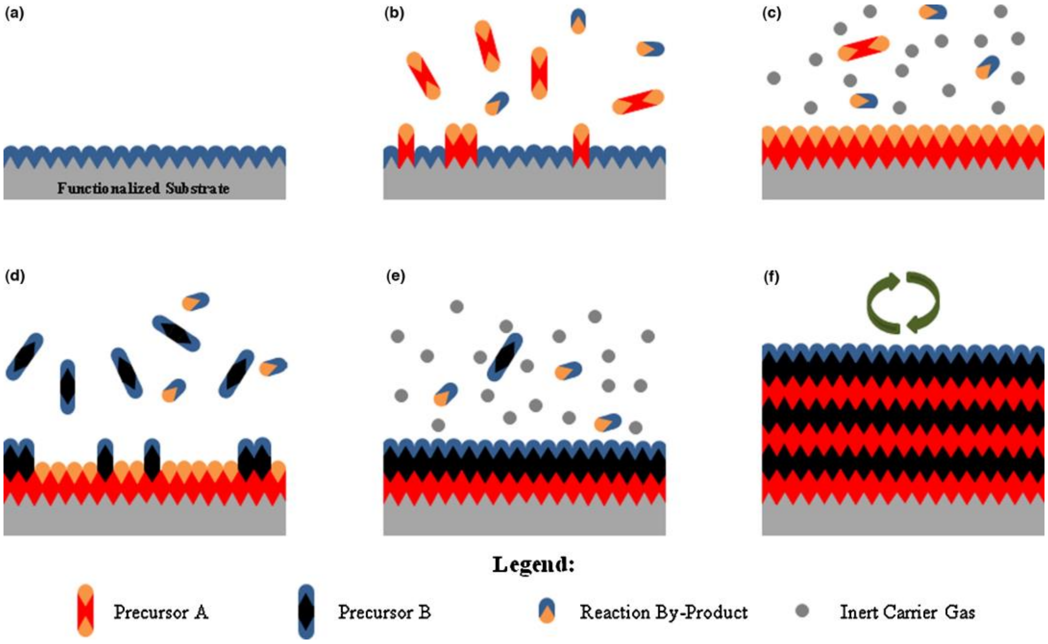

Figure 1. Schematic representation of an ALD process. (a) substrate before deposition, (b) first precursor is introduced to the surface, (c) excess precursor and byproducts are purged away, (d) second precursor is introduced to the surfacce, (e) excess precursor and byproducts are purged away, (f) cycles are repeated until desired film thickness is deposited. Reprinted from [11], © 2014, with permission from Elsevier.

Because the reactions are self-limiting, films made with ALD are very conformal, meaning that they have uniform thickness everywhere on the substrate surface.[10] This conformality makes the method very attractive for depositing thin films on complex substrates and for making interfacial layers, which often need to be very thin but still pinhole free. The controllability of ALD also makes it ideal for depositing ultrathin layers. Films can also be doped in a very controlled manner by sequential addition of dopant precursor pulses to the process.[12] On the other hand, ALD is quite slow compared to other thin film deposition methods, but batch processing can ensure high throughput. The low growth temperatures can also often result in amorphous films that might need additional processing steps such as annealing.[13]

In addition to purely thermally activated chemicals, plasma species can be used as precursors. For example, oxides are usually grown using either H_2O or O_3 as the oxygen precursor, but in plasma-enhanced ALD (PEALD) O_2-plasma is used instead.[14] The added energy allows for deposition of many materials at lower temperatures as compared with thermally activated ALD, and the reactive plasma species can more efficiently break down adsorbed precursor fragments that could incorporate into the films as impurities, which leads to purer films.[14] The downsides of PEALD are that the conformality of deposited films is generally worse, the substrate and the film are also exposed to potentially damaging ion bombardment, and the chemistry of plasma processes is more complicated than that of thermal processes.[14]

Regarding semiconductor materials in photocatalysis, ALD is advantageous for fabricating interfacial layers and modification layers and for depositing semiconductor films on nanostructured surfaces.[15] $BiVO_4$ in particular benefits from nanostructures, as its charge transport characteristics are not compatible with the large optical thicknesses needed for efficient light harvesting.[16] Three processes for depositing $BiVO_4$ with ALD have been reported before, two of which result in non-stoichiometric films that need annealing and chemical treatments after the deposition.[17,18] The third process does not have this drawback, but it is based on nanolaminates of the binary oxides that still need to be annealed to form the final film.[19]

The literature part of this work summarizes the basic principles of semiconductor photocatalysis, the different classes of semiconductor materials used in photocatalysis, and the various strategies used to improve their performance. Special attention is paid to $BiVO_4$, and the existing $BiVO_4$ ALD processes are thoroughly reviewed. The goal of experimental work in this study was to develop a new ALD $BiVO_4$ process for use in semiconductor photocatalysis. By combining two existing V_2O_5 and Bi_2O_3 ALD processes it was possible to deposit $BiVO_4$, but an annealing step was necessary to obtain thin films with semiconducting properties. The deposition process and characterization of the films are detailed in the experimental section of this thesis.

2 Principles of photocatalysis

2.1 Band structure of semiconductors

Semiconductors and insulators are characterized by a density of electronic states where the highest occupied states and the lowest unoccupied states form distinct energy bands separated by a gap of forbidden energy levels with specific band gap energy, E_{gap}.[20] An example of a semiconductor energy diagram is presented in Figure 2. Semiconductors are differentiated from insulators by the band gap energy, and materials with $E_{gap} > 4$ eV are generally regarded as insulators.[20] Each material also has a characteristic Fermi level (E_F), which along with temperature determines the electron distribution in the bands, because electron density is a product of the Fermi-Dirac distribution and the density of states in the semiconductor.[21] Above 0 K electrons are thermally excited to the conduction band and leave electron vacancies in the valence band. The vacancies act as virtual particles with a positive charge and are known as holes. The mobile electrons and holes impart conductivity to semiconductor materials.[21]

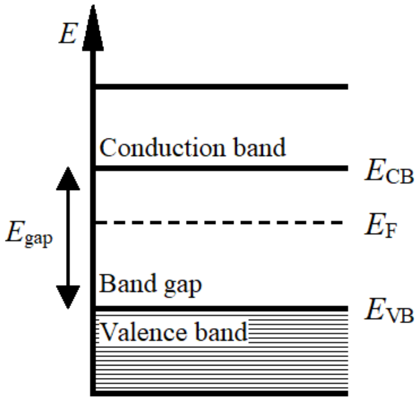

Figure 2. Band diagram of a semiconductor.

The Fermi level is shifted to higher or lower energy levels by donor or acceptor states in the semiconductor.[21] With a high E_F the distribution of electrons is shifted upwards, and so there are more electrons in the CB than holes in the VB. This kind of a material that has electrons as the majority carrier is called n-type, whereas a material with low E_F and, consequently, holes as the majority carrier is called p-type. The donor and acceptor states that are needed to make a material n- or p-type can result from intrinsic defects and impurities in the material, or they can be introduced purposefully through doping with foreign elements to modify the semiconducting properties.

Semiconductors can also be categorized to direct and indirect band gap materials.[21] In the direct band gap materials, the VB edge and CB edge are aligned in the momentum space, which means that no extra energy beyond E_{gap} is needed for the electron transition. In materials with an indirect band gap, by contrast, the band edges are not aligned, and a momentum transfer between the electron and the crystal lattice must take place through absorption or creation of a phonon. This requirement decreases the probability of absorption and thus makes the absorption less efficient. Conversely, recombination is also slower in indirect band gap materials.[7]

2.2 Photocatalysis and photoelectrocatalysis

When a photon is absorbed by a semiconductor, the generated electron-hole pair has energy that can be used to power chemical reactions in photocatalysis. Two important aspects of the band gap with respect to photocatalysis are its energy and the band edge positions. The electrons in the conduction band need to be at a more negative electrochemical potential than the reduction potential of the intended reaction, and the holes in the valence band need to be at a more positive potential than the concurrent oxidation reaction. This requirement is demonstrated in Figure 3 with a schematic representation of the band edges of a semiconductor photocatalyst suitable for water splitting. To overcome resistance at various parts of the process, an overpotential μ is also needed.[22] It should be noted that in photocatalysis overpotential is sometimes used to refer to the difference between the band edges and the respective redox potentials.[23]

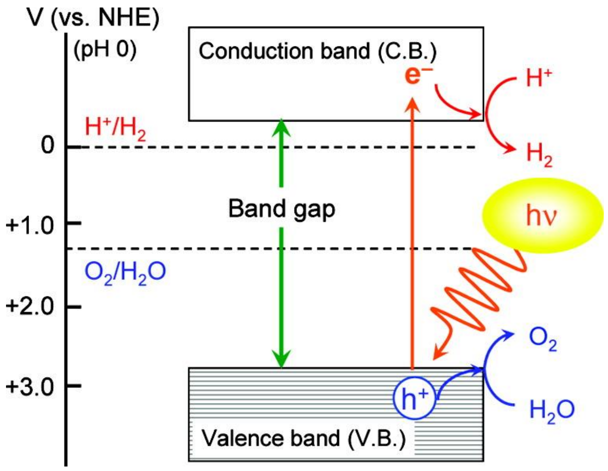

Figure 3. Schematic representation of the photocatalytic splitting of water. Reprinted with permission from [24]. © 2007 American Chemical Society.

For reaching the required electrochemical potentials, a large band gap energy is beneficial. However, a large band gap requires high energy photons for the electron-hole pair production, which limits the spectrum of light that is absorbed. For most applications, it is desirable to minimize the band gap to increase the proportion of light that can be utilized. Of course, the band edges should also be correctly located in relation to the reaction potentials. Finding a single semiconductor that fulfills these requirements is not a simple task, and some sort of compromise is usually necessary.

In photocatalysis, the semiconductor is generally employed as a powder or in some other particulate form. This approach affords several benefits, such as simplicity and easy scaling. In photoelectrocatalysis, on the other hand, a semiconductor photocatalyst is used as either one or both electrodes in an electrochemical cell. n-type semiconductors are used to make photoanodes and p-type semiconductors as photocathodes.[23] The physical separation of the oxidation and reduction reactions has the benefit of inhibiting reverse reactions and recombination. An external bias voltage, which shifts the band potentials and enhances charge separation in the semiconductor, can also be applied, but it requires external energy input

2.3 Factors affecting the efficiency of photocatalysis

Efficiency of a photocatalytic system is a product of multiple factors: light absorption efficiency, charge separation efficiency, and charge injection efficiency. These factors are affected by basically everything in the system: the intrinsic properties of the semiconductor, modifications like doping, physical properties such as shape and size of the photocatalyst, and the chemical reaction and environment. Efficiency of a heterogeneous photocatalyst is commonly reported either by quantum efficiency (QE) or quantum yield (Φ). QE is the rate of a photochemical process divided by the total absorbed photon flux, and Φ is the number of photochemical events divided by the number of photons *absorbed* at a specified wavelength. Apparent quantum yield (AQE) is also used, and it is the number of photochemical events divided by the number of *incident* photons at a certain wavelength.[25]

The efficiency of a photoelectrochemical system is typically reported in terms of incident photon to current efficiency (IPCE, also external quantum efficiency EQE), which is the ratio of the generated electric current to the incident photon flux. By measuring the reflected and transmitted photons and subtracting their numbers from the incident photon flux, absorbed photon to current efficiency (APCE, also internal quantum efficiency IQE) can be calculated. It is a measure of the internal efficiency of the system.[26] IPCE and APCE are measured as a function of the wavelength and should not be confused with the overall energy conversion efficiency.

The ratio of absorbed to incident photons is the light absorption efficiency of a photocatalytic system. Factors that affect it are surface reflectance, optical thickness, and the wavelength dependent absorption coefficient of the photocatalyst material, which in turn is determined by the band structure of the semiconductor.[7] In aqueous photocatalysis the semiconductor is typically a suspended powder, and as such, it is rather simple to scale the system dimensions to harvest close to all the light with photon energies larger than the band gap.

In photoelectrodes, on the other hand, scaling the system is far less straightforward, as simply manufacturing a thicker absorption layer leads to losses due to impaired charge transport to the catalytic surface and the conductor.[18] Electron and hole mobilities in semiconductors are often different, and even the direction from which the electrode is illuminated sometimes makes a difference in the operating efficiency.[27] The optical thickness of an electrode can be decoupled from the semiconductor layer thickness, however, by utilizing a porous structure of transparent and conductive material on which the semiconductor layer is deposited. These so-called host-guest architectures will be discussed further in a following chapter.

Charge separation efficiency is the measure of how many photogenerated carriers reach the catalyst surface without recombining. The recombination rate is affected by intrinsic carrier mobility in the semiconductor and by defects that can lower the mobility or act as recombination sites. Elementary processes in photocatalysts are demonstrated in Figure 4. Charge separation can be enhanced by doping to increase carrier mobility and by constructing heterostructures or interfacial layers that create internal electric fields which drive the opposite charges apart. In photoelectrocatalysis a bias voltage is also applied as mentioned above.

After the charge carriers reach the catalyst interface, they still need to cross over the semiconductor-liquid interface and react to form the desired products. Kinetics plays a key role in determining the charge injection efficiency as recombination or trapping of carriers can occur

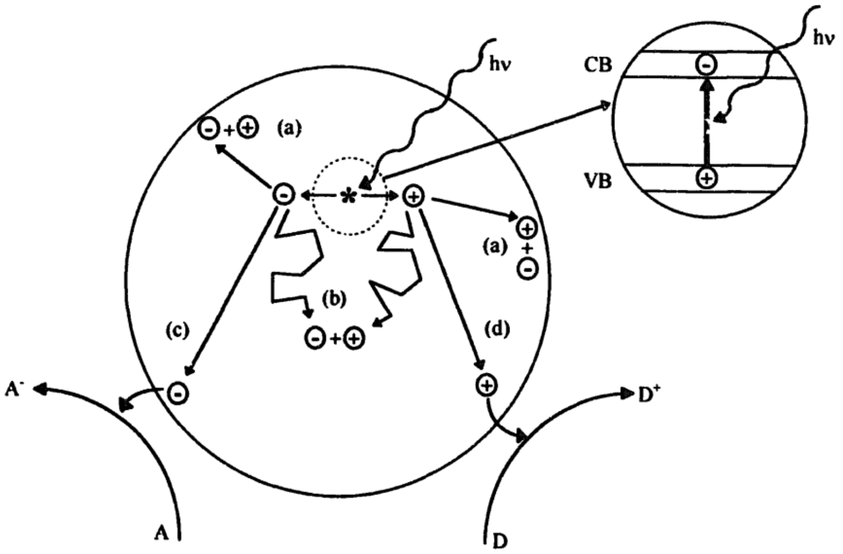

Figure 4. Elementary processes in semiconductor photocatalysis. Recombination of electrons and holes a) at the surface and b) in the bulk, c) reduction of an electron acceptor by a photogenerated electron and d) oxidation of an electron donor by a photogenerated hole. Reprinted from [270], © (1997), with permission from Elsevier.

in the range of 10 ns, whereas the timescale of charge injection is on the order of 100 ns and that of surface reactions on the order of milliseconds.[28] Thus, the rate of the reaction on the surface can become a limiting factor for the overall efficiency. Adsorption and desorption rates of the reactants and products must also be considered, as the number of active sites on the catalyst surface is limited, and the surface might get poisoned if the product lingers on the surface or readsorbs. Accordingly, if the reactant adsorption is slow or desorption fast, the active sites are left empty. Some methods for increasing surface reaction rates are doping,[29] using cocatalysts,[30] and modifying the crystal facets exposed on the surface.[31]

The charge separation efficiency and charge injection efficiency together determine the APCE of a photoelectrocatalytic system. To study them separately, sacrificial reagents that are selected for their quick reactions are be used. The charge injection efficiency can then be assumed to be 100 %, and the wavelength dependent charge separation efficiency of the system is obtained as the APCE.[18] Sacrificial reagents are often also used to characterize overall conversion rates in photocatalytic systems, but in this case care should be taken not to draw false conclusions. For example, in H_2-generating systems sacrificial hole scavengers can increase the H_2 production through a process known as current doubling, where both the photogenerated electrons and holes participate in hydrogen formation.[32]

Two more efficiency lowering processes are back reaction[33] and photocorrosion.[34] Back reaction can happen if the products react with each other or if they can react with the photogenerated charge carriers to regenerate the reactants. The impact of back reactions on the efficiency is highly dependent on the chemical species in question. If the back reaction it is a problem, the spatial separation of products afforded by photoelectrocatalysis is advantageous. Photocorrosion means that the photogenerated electrons or holes also reduce or oxidize the catalyst itself, leading to decreased charge injection efficiency and, more importantly, to eventual degradation of the catalyst. In this case, using scavenger species can help. Another option is to add a protective layer that allow charge transport but prevent dissolution of the semiconductor.

3 Semiconductor materials

The previous chapter introduced several requirements that a semiconductor should ideally satisfy to maximize its efficiency as a photocatalyst. In addition to having the proper physical properties, a good semiconductor material should ideally consist of earth-abundant elements and be inexpensive to manufacture in a large scale. A prime example of a semiconductor used in photocatalysis is TiO_2, which has been widely adopted in commercial applications and is arguably the most widely studied photocatalyst material.[35,36] Despite the development of more efficient materials, TiO_2 is still important by the virtue of its excellent stability and affordability.

Although dominating the commercial space in photocatalysts, TiO_2 is far from being the only viable option currently under research. Multitudes of other metal oxides, nitrides, halides, oxynitrides, oxyhalides and chalcogenides, and group IV and III-V semiconductors have been demonstrated to be photocatalytically active, each with its strengths and weaknesses. Figure 5 compares the band edge potentials and band gap energies of various semiconductors.

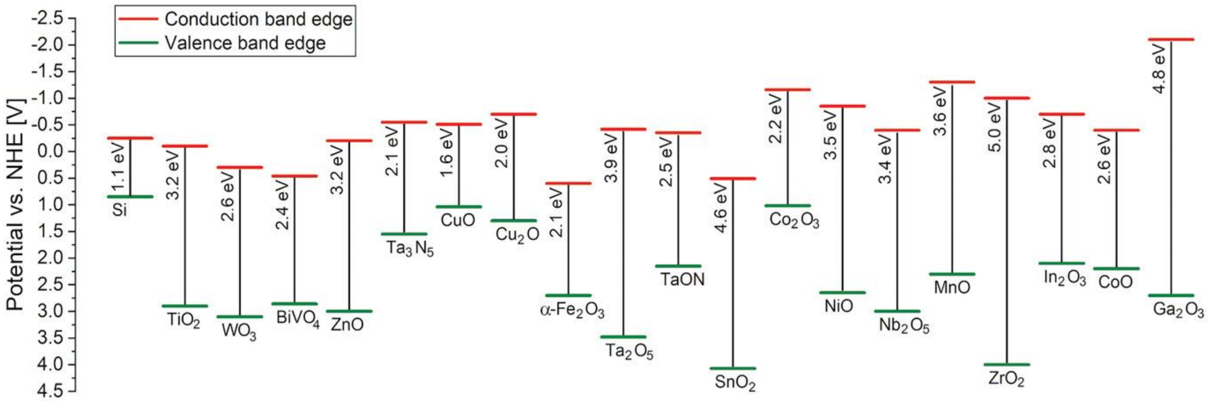

Figure 5. Band edge potentials vs. normal hydrogen electrode (NHE) and band gap energies of selected semiconductors. Reprinted with permission from [15], © 2021 Wiley-VCH GmbH.

The following three chapters will survey the different materials used in photocatalysis so far, starting with oxides, followed by nitrides, oxynitrides, chalcogenides, and oxyhalides, and finishing with the group IV and III-V semiconductors. Because the conditions used to measure photocatalytic activity are often disparate and the photocatalyzed reactions are diverse, no comparison of the overall effectiveness of different photocatalysts is attempted. Instead, the focus is on qualitative comparison of material properties and general trends.

3.1 Metal oxide semiconductors

Metal oxides are likely the largest group of materials studied for photocatalysis. This is mostly due to their inherent stability in water and resistance to photocorrosion, although the stability also varies a lot among the different oxides. Disadvantages of oxides are that they generally have larger band gaps than other materials and they suffer from poor carrier transport. Oxides are typically n-type semiconductors due to the presence of oxygen vacancies, but there are also p-type oxides, such as Cu_2O.[37] Properties of selected metal oxides are presented in Table 1.

Table 1. Band gaps and charge transport properties of selected oxide semiconductors. μ is the mobility of a charge carrier and *L* the diffusion length of charge carriers. Reproduced with permission from [38], © 2018 WILEY-VCH Verlag GmbH & Co. KGaA, Weinheim.

Material	**E_g (eV)**	**Band gap type**	**μ (cm^2/Vs)**		***L* (nm)**	**Ref.**
			Electron μ_n	**Hole μ_p**		
TiO_2, rutile/anatase	3.02/3.20	Direct/indirect	0.01	100	10–100	[39,40]
WO_3	2.8	Indirect	10	20–104	150–500	[16,41]
ZnO	3.37	Direct	130–440	0.1–50	130–440	[42,43]
$SrTiO_3$	3.25–3.75	Indirect/direct	10^3–10^4	0.1	100–1000	[44–47]
$BiFeO_3$	1.82–2.27	Indirect/direct	–	10^{-7}	3.5	[48,49]
Fe_2O_3	1.9–2.2	Indirect	0.5	10^{-7}–10^{-4}	2-4	[50,51]
Cu_2O	2.14	Direct	6	256	25	[16,52]
$BiVO_4$	2.4	Indirect	0.044	2	70	[53,54]

Metal oxides with cations in either d^0 or d^{10} electron configuration are generally favored in the overall photocatalytic water splitting, where both O_2 and H_2 are generated by the same semiconductor.[24] They give rise to conduction bands consisting of empty d-orbitals or hybridized s- and p-orbitals of the cations, respectively. Although there is concern about the partly filled d orbitals of other cations acting as recombination centers[55], some of their oxides (e.g. Fe_2O_3) have also been studied for various photocatalytic applications.[56] The valence bands of oxide semiconductors, in turn, are generally composed primarily of the oxygen 2p orbitals, which are located at very positive potentials (+3 V vs. SHE).[2] Exceptions to this trend include $BiVO_4$, where Bi 6s orbitals significantly contribute to both the valence and conduction bands, making the valence band edge less positive and lowering the band gap energy.[7,53]

The low band gap energy of 2.4–2.5 eV means that $BiVO_4$ can absorb photons with wavelengths shorter than about 500 nm.[7] The absorption edge of $BiVO_4$ is therefore well in the visible light range (380–760 nm according to ISO standard 21348)[57]. Although the conduction band edge is slightly too positive (ca. 0 V vs. NHE) to facilitate the water reduction necessary for the overall water splitting, the valence band edge is well below the water oxidation potential and provides ample thermodynamic driving force for the reaction.[58] The fundamental band gap of $BiVO_4$ is indirect, which slows down carrier recombination somewhat, whereas a direct band gap just 0.200 eV above the fundamental transition (Figure 6) gives rise to strong optical absorption near the absorption edge.[7] The main limiting factor of $BiVO_4$ is a rapid surface recombination rate of charge carriers, but it can be mitigated by co-catalysts and other surface modifications.[59,60] Charge transport in $BiVO_4$ is also rather slow, but it is compensated for by long carrier lifetimes[16] and can be enhanced by doping.[61]

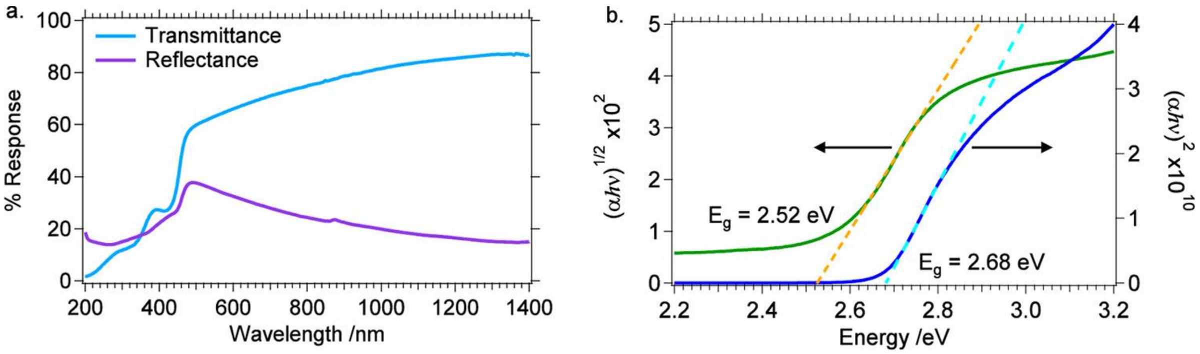

Figure 6. a) Transmittance and reflectance spectra of $BiVO_4$. b) Tauc plots for determining the indirect and direct band gap values of $BiVO_4$. Reproduced with permission from [7]. Copyright 2015 American Chemical Society.

Although some oxides boast an even lower band gap than $BiVO_4$, their intrinsic properties fall short in other areas. Cu_2O has a band gap of just 2.14 eV with a proper conduction band edge position for reduction of water and CO_2, but it is notorious for photocorrosion by oxidation to CuO or reduction to Cu.[62,63] Still, as a p-type oxide, Cu_2O a is very useful photocathode material for photoelectrocatalytic systems because most of the widely studied oxides are intrinsically n-type.[64] The use of Cu_2O requires, however, that additional measures are taken to protect the catalyst during operation.[65] Alternatively, ternary and quaternary compounds derived from Cu_2O, such as $CuFeO_2$,[66] Cu_3VO_4,[67] and $CuAlO_2$,[68] are possibly more stable, but their band structures can be very different from that of Cu_2O, even to the point that any advantage compared with other oxide materials is lost.[64]

Another prominent oxide with a low band gap is α-Fe_2O_3. It is non-toxic and very abundant, making it highly attractive from the environmental and production standpoints. α-Fe_2O_3 is also very stable, unlike Cu_2O, but the main downside of this material is its poor carrier transport.[56] Pure α-Fe_2O_3 is in fact highly insulating,[69] and dopants are needed to make it conductive enough for photocatalysis. Some dopants that have been used to increase the efficiency of Fe_2O_3 include niobium,[70] silicon,[71] and titanium,[72] although Zandi et al.[72] attributed the increased efficiency with Ti^{4+} to improved interfacial charge transport rather than electrical doping. Figure 7 displays some of their results.

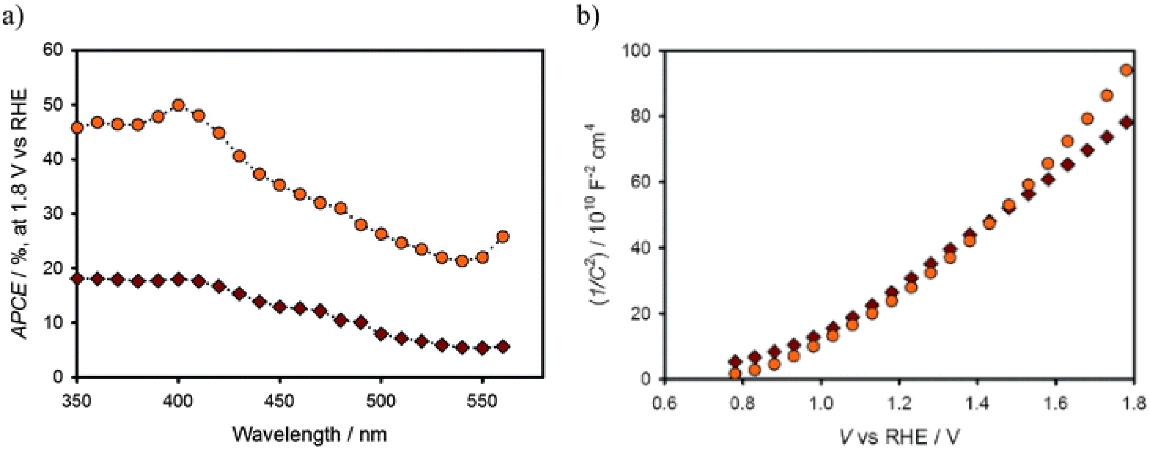

Figure 7. a) APCE spectra and b) Mott-Schottky plots of undoped (dark red diamonds) and Ti-doped (orange circles) Fe_2O_3 showing the increased effciency with doping while the charge carrier density remains similar in the two samples. Used with permission of The Royal Society of Chemistry, from [72]; permission conveyed through Copyright Clearance Center, Inc.

The stability of iron oxides has also directed attention to some ternary iron oxides. Perovskite $BiFeO_3$ has mostly been studied in other fields for its multiferroic properties,[73] but its suitability as a photocatalyst has also been recognized. The conduction band edge of $BiFeO_3$ is not at a suitable potential for hydrogen production,[74] but it is active for oxygen evolution[75] and dye degradation.[76,77] Hydrogen evolution under visible light has also been achieved with a composite $SrTiO_3$/$BiFeO_3$ photocatalyst with CH_3OH as a hole scavenger.[78] It seems, however, that on their own iron-based photocatalysts are limited by poor charge carrier mobility, high rate of surface recombination, and slow water oxidation kinetics.[56] Therefore it is reasonable to assume that other materials would serve better in heterostructures as well.

Of the wider band gap semiconductors WO_3,[79,80] TiO_2,[55] ZnO,[81] and $SrTiO_3$[82] have been researched extensively. Studies on ZnO have focused particularly on degradation of organic pollutants in wastewater,[83] whereas the other three materials have been studied in wider fields of applications. WO_3 is relatively inactive as a standalone photocatalyst[84] but has been employed in heterostructures with, for example, TiO_2[79] and graphitic C_3N_4.[80] $SrTiO_3$ is another perovskite material that has been used for photocatalysis. It has properties similar to TiO_2 in many respects, but its conduction band edge is about 0.4 eV more negative,[85] and so provides more potential for H_2 generation. Other perovskite type titanates, such as $BaTiO_3$,[85] have also been studied, but the wide band gap generally remains an issue.

Because of the wide band gaps, UV light is required for photoexcitation of TiO_2, $SrTiO_3$, and ZnO. Even WO_3 can absorb only a small part of the visible spectrum. In many applications, such as self-cleaning and -sterilizing surfaces,[4,86] low absorption is not a problem, as maximizing the portion of incident light absorbed is not that crucial for the operation. In applications like water splitting, however, the limited absorption greatly decreases efficiency. Moreover, the large band gaps generally result in unnecessarily large potentials in comparison to the redox potentials of the reactions, which essentially means that a portion of the absorbed energy is wasted. Use of additional catalysts or doping can widen the light absorption range to the visible region and enhance charge separation, but doping also involves the risk of increasing the number of recombination sites in the photocatalyst.[62,87,88]

3.2 Metal nitrides, oxynitrides, chalcogenides and oxyhalides

The band gaps of oxides capable of hydrogen production are generally very wide because of the positive potentials of valence band edges formed by the O2p orbital, which is why materials with other anions have been studied as alternatives. Metal nitrides and sulfides, for example, tend to have valence bands with less positive edges.[24] For the same reason, nitrogen and sulfur are often used as dopants to adjust the valence band edge of oxides.[89] Another addition to the selection of mixed anion photocatalysts are layered bismuth oxyhalides and materials derived from them by addition of different metal oxides.[90] Table 2 introduces properties of selected non-oxide semiconductors.

Table 2. Band gaps and charge transport properties of selected non-oxide semiconductors. Parts of table reproduced with permission from [38], © 2018 WILEY-VCH Verlag GmbH & Co. KGaA, Weinheim.

Material	E_g	**Band gap type**	**μ (cm²/Vs)**		***L* (μm)**	**Ref.**
			electron μ_n	**hole μ_p**		
$BaTaO_2N$	1.9–2.0	Direct	–	–	–	[91,92]
Ta_3N_5	2.01/2.12	Indirect/direct	1.3–4.4	0.08	18	[93–96]
TaON	2.08/2.4	Indirect/direct	17-21	0.01	8	[94,97]
CdS	2.42	Direct	300	6–48	0.275	[98]
CdSe	1.74	Direct	450–900	10-50	0.06–0.11	[99]
CdTe	1.5	Direct	1100	100	0.4–1.6	[100]
$CuInS_2$	1.42–1.81	Direct	240	15	0.4–1.25	[101–103]
ZnS	3.66	Direct	–	–	0.15	[104,105]

Though the contributions of different elements on the band gap are not necessarily straightforward, the effect of nitrogen content on the valence band edge is seen particularly well in the band edge positions of Ta_2O_5, TaON, and Ta_3N_5 as presented in Figure 8. The conduction band edges of the three materials are close to each other, but the valence band edge moves towards less positive potentials as the nitrogen content is increased.[106] Consequently, the band gap gets narrower, and TaON and Ta_3N_5 absorb in the visible wavelength, whereas the band gap of Ta_2O_5 is so wide that it is unlikely to be considered as a photocatalyst. The cause of this shift by the N2p orbitals is also corroborated by density functional theory (DFT) calculations.[107]

Ta_3N_5 and TaON are the foremost nitride materials studied for photocatalysis. They can be very simply prepared by heating Ta_2O_5 in an NH_3 atmosphere,[106] and more importantly, the narrow band gaps and proper band edge positions make TaON and Ta_3N_5 very attractive for overall water splitting. The main concern is the oxidation of the nitride anions to N_2 by the photogenerated holes.[34] By using sacrificial reagents, both H_2 and O_2 production have been individually demonstrated with TaON, and only slight decomposition of the catalyst at the start of the photocatalysis was observed in neutral buffered solution.[108] Similar results were obtained for Ta_3N_5, but Hara et al.[109] noted that operation at $pH < 7$ resulted in decomposition of both catalysts. Overall water splitting was not achieved because the rate of H_2 evolution was low compared with the rate of O_2 evolution.[108,109]

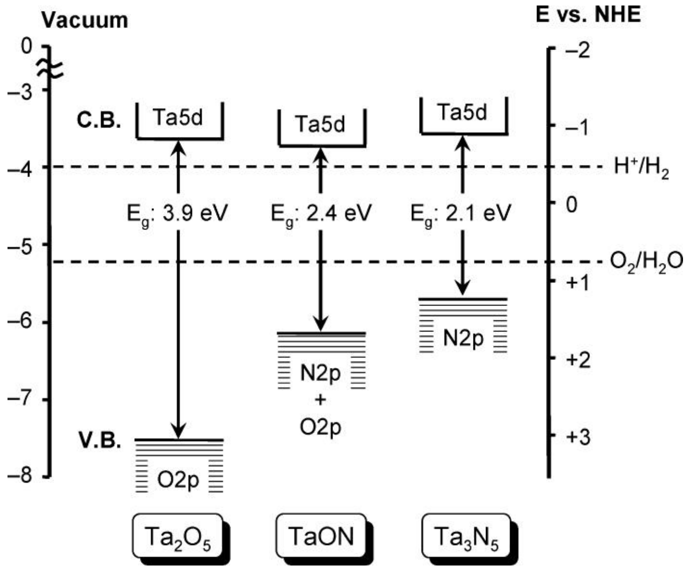

Figure 8. Energy band diagrams of Ta_2O_5, TaON and Ta_3N_5 showing the negative shift of valence band edge as nitrogen content increases. Left scale shows the potentials against vacuum level. Reprinted with permission from [24]. © 2007 American Chemical Society.

A group of oxynitrides derived from TaON are $ATaO_2N$ perovskites, where A is Ca, Sr, or Ba. The band structure of these perovskites is very sensitive to the size of the alkali metal cation, and with these materials the conduction band edge can also be tuned to some extent.[91] $BaTaO_2N$ in particular has been studied for overall solar water splitting. It photocatalyzed the H_2 evolution somewhat faster than TaON or Ta_2N_5,[110] and W doped BaTaON with IrO_2 cocatalyst evolved O_2 as well when Ag^+ was used as a sacrificial reagent.[111]

Another nitride material that has received attention for the photocatalytic water splitting is the solid solution of GaN and ZnO, $(Ga_{1-x}Zn_x)(N_{1-x}O_x)$.[112] Even though both of the constituents have band gap energies larger than 3 eV, the band gap energies of the solid solutions are in the range 2.4–2.8 eV, depending on the value of x. As such the solid solutions are not active for the water splitting but they do show evolution of both O_2 and H_2 with the addition of a RuO_2 cocatalyst.[113] Stability in basic solutions is poor, but in a solution with pH 4.5 $(Ga_{1-x}Zn_x)(N_{1-x}O_x)$ with a $Rh_{2-y}Cr_yO_3$ cocatalyst retained its initial rate of water splitting for more than 90 days. By 180 days the rate had dropped to 50 % of the initial value.[114]

The valence band edges of metal sulfides and other chalcogenides are also generally less positive than those of oxides, and many of them have intrinsically narrow band gaps. In addition, the quantum yields of many sulfides are exceptionally high: ZnS reached a quantum yield of 90 % for hydrogen production under UV light.[104] Chalcogenides are, however, very prone to photocorrosion, with the sulfide anion oxidizing to elemental sulfur or sulfate. Photocorrosion can be avoided by using sacrificial hole scavengers in the photocatalysis solution. CdS and CdSe, for example, are stable in solutions containing free S^{2-} or SO_3^{2-} ions.[115] CdTe is not stable in these solutions and requires Te^{2-} in the solution.[116] Sacrificial solutions come with a few downsides: they require periodic replenishment, and the oxidized species might decrease the efficiency through back reactions with photogenerated electrons.[104] Some other chalcogenides used in photocatalysis include $CuInS_2$,[117] $Cu(In,Ga)Se_2$,[118] MoS_2,[119] and Bi_2S_3.[120] The latter two have received attention especially as cocatalysts or as parts of heterostructures.[121–123]

Layered bismuth oxyhalides have shown photocatalytic activity in dye degradation. BiOCl and BiOBr with band gaps of 3.4 and 2.8 eV, respectively, decomposed methyl orange, and BiOCl was more active than a commercial TiO_2 photocatalyst.[124,125] Because of the layered structure, which is shown in Figure 9, charge transport in bismuth oxyhalides is highly anisotropic, and it has been shown that charge separation is enhanced in the [001] direction.[126,127] As a result, the photoactivity of single crystalline BiOX nanosheets is correlated with the proportion of {001} facets exposed. Similar to other non-oxide materials, stability of bismuth oxyhalides is a concern. BiOX derivatives of the form $Bi_xMO_yX_z$ (where M is Nb, Ta, Sr, Gd, or Pb) have been synthesized and show alterations to the band structure and increased stability against photocorrosion.[90,128]

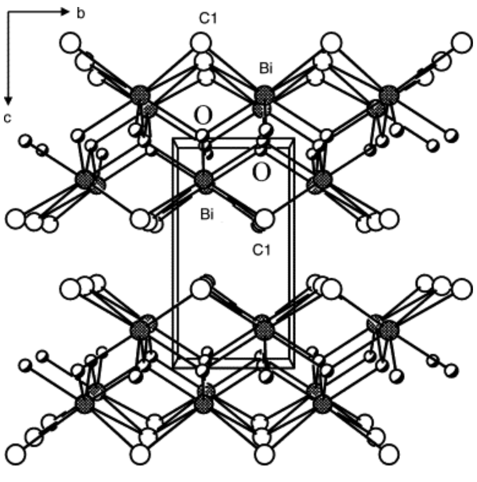

Figure 9. Crystal structure of BiOCl with the unit cell drawn in. Reprinted from [125], © 2006, with permission from Elsevier.

3.3 Group IV and III-V semiconductors

Group IV and III-V semiconductors are commonly used in integrated circuits and photovoltaic applications. Because of the long history of research, methods to manufacture these materials in very high quality, such as the Czochralski method,[129] are available. Defect free materials have excellent charge transport properties as can be seen in Table 3. Charge carrier diffusion length in silicon, for example, is on the order of 100 µm,[130] whereas for oxides this value is typically in the sub-µm range. In addition to that the Group IV and III-V semiconductors are easily doped to both n- and p type, which makes it straightforward to form homojunctions that enhance charge separation.[131] They also have rather low band gaps, which increases absorption and carrier density but also means that one or both band edges are at too low potentials to work without external bias. By far the biggest drawback of these materials is, however, their vulnerability to photocorrosion.[132,133] Therefore, they need protective layers to prevent the degradation, which adds more interfaces that may have efficiency-lowering defects.

Table 3. Band gaps and charge carrier properties of silicon and selected group III-V semiconductors. Reproduced with permission from [38], © 2018 WILEY-VCH Verlag GmbH & Co. KGaA, Weinheim.

Material	E_g	**Band Gap type**	**µ (cm^2/Vs)**		L **(µm)**	**Ref.**
			electron μ_n	**hole** μ_p		
Si	1.12	Indirect	1400	500	100	[130]
GaAs	1.43	Direct	8500	400	100–900	[131]
GaP	2.26	Indirect	250	150	1–10	[134]
InP	1.35	Direct	5400	160	12	[135]
$Ga_xIn_{x-1}P$	1.34–2.6	Direct	400–2000	35	2	[136,137]

Despite being the most widely used material in photovoltaics, silicon is quite rarely studied for direct photocatalysis, which is indicative of how much it suffers from the photocorrosion in aqueous solutions. This susceptibility has led to the development of buried junction photoelectrochemical cells that have the silicon completely covered by a conductive protective layer, on top of which a redox catalyst is deposited.[132] The band gap of silicon is just 1.1 eV, which means that it does not have enough potential for the overall water splitting.[38] Essentially, the buried junction forms a photovoltaic cell, and the photovoltage is used in addition to an applied external voltage or another photoelectrode in electrolysis and photoelectrocatalysis, respectively. A 0.5 V decrease in the onset voltage of water oxidation was observed upon illumination of this kind of a photoelectrode.[132] The cocatalyst can also be deposited directly on the silicon where it also acts as a protective layer, but the interface needs to be engineered to ensure good charge transport.[138]

III-V semiconductors that have been used for photocatalysis include GaAs, GaP,[139] InP,[140] and $Ga_xIn_{x-1}P$,[141] among others. They share many of the benefits of highly pure elemental semiconductors but offer more choices for band gaps and different interfacial properties with protective layers and cocatalysts. The band gap of $Ga_xIn_{x-1}P$ can be tuned by varying the ratio of Ga and In.[142] $Ga_{0.5}In_{0.5}P$ has a band gap energy of 1.83 eV,[141] which makes it a viable material for the overall water splitting. In comparison to silicon, however, III-V semiconductor devices are considerably more expensive to manufacture.[143]

4 Strategies to improve efficiency of photocatalysts

The purpose of this chapter is to describe principles of the most common modification methods that are used to enhance efficiency of photocatalytic and photoelectrocatalytic systems and overcome the shortcomings of various semiconductor materials. Special attention is paid to the modification of $BiVO_4$ photocatalysts and photoanodes. This survey will be limited to simple inorganic materials, but it should be noted that multiple other methods, such as metal-organic frameworks[144], dye-sensitization of surfaces[145], and surface plasmon resonance enhanced catalysis[146] show promising developments in the field.

4.1 Nanostructures

Shaping photocatalyst materials into nanostructures to improve photocatalytic activity is conceptually simple but the implementation can range from simple etching to multi-stage deposition processes. Some examples are etching of silicon to create nanorod arrays[147], chemical vapor deposition of nanostructured silicon-doped Fe_2O_3 films with dendritic nanostructure[71], and atomic layer deposition of $BiVO_4$ thin films on antimony-doped tin oxide nanotubes with ALD SnO_2 underlayers.[148]

Nanostructuring increases the surface area to mass ratio of the photocatalyst. This means that more charge carriers are generated close to the surface, and therefore the average distance they need to travel to reach the surface is decreased. A larger specific surface area also increases the adsorption area and decreases the current density while retaining or increasing the current density for the projected surface area of the device. The low current density better matches the surface reaction rates, which are generally slow compared with the charge transfer as discussed in chapter 2.3. Unfortunately, the number of the efficiency-lowering surface trapping sites is also increased, but there is a reason to believe that surface treatments can decrease the density of such defects. For example, the commonly utilized chemical treatment of silicon by oxidation and HF-etching results in very low surface recombination velocity.[149] A study on mesoporous silicon nanoparticles for photocatalytic hydrogen evolution revealed that an optimum concentration exists for the HF-treatment solution.[150] More concentrated HF solutions resulted in morphological damage and adsorption of byproducts, which increased recombination. One might also consider some surface cocatalysts and interfacial layers to fall into the category of surface treatments. They will be discussed further in their own chapter.

Attention should also be given to the crystallographic planes exposed on a semiconductor surface because in some materials the charge transfer characteristics can be highly anisotropic.[71,126,127] Different surface facets also have slightly different electronic structures, which can promote charge separation on different facets. This was demonstrated experimentally by Li et al.,[31] who photodeposited noble metals and metal oxides on $BiVO_4$. They found that photogenerated electrons and holes migrate to the {010} and {110} facets, respectively, leading to photoreduction deposition of noble metals on the {010} facets and photo-oxidation deposition of metal oxides on the {110} facets (Figure 10).

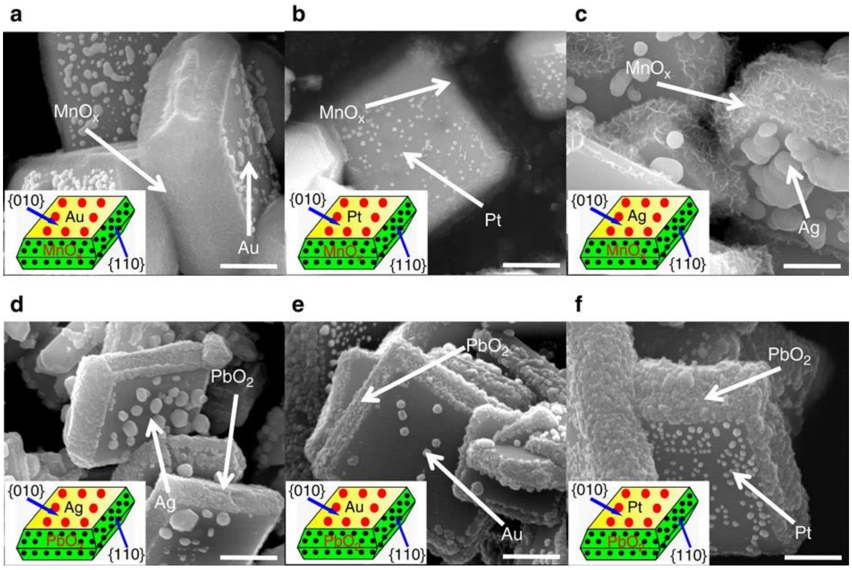

Figure 10. SEM image of simultaneously photodeposited noble metals and metal oxides on crystalline $BiVO_4$. Reprinted from [31] with permission from Macmillan Publishers Limited, © (2013).

Another result from surface nanostructures is increased roughness that can lead to increased scattering of reflected light into the structure. Thus, the incident light has more chances to absorb, which leads to increased efficiency. This effect was attributed to be one of the main benefits of one-dimensional silicon nanostructure arrays studied by Wu et al.[147] The flip side of increased surface area pertaining to light absorption is that the absorbed photon flux per unit area of the photoelectrode is decreased, which leads to lower voltage according to the Shockley diode equation:

$$V_{\mathrm{OC}} = \frac{kT}{e}\ln\left(\frac{J_{\mathrm{phot}}}{J_0} + 1\right), \tag{1}$$

where V_{OC} is the open circuit potential, J_{phot} is the absorbed photon flux, and J_0 is the reverse saturation current. The voltage decreases by 0.059 eV when the absorbed photon flux is reduced by a factor of 10,[151] and the lower voltage results in smaller thermodynamic driving force for photocatalytic reactions.

When the nanostructures are small enough, the electronic structures of semiconductors are also affected. In structures with dimensions of a few nanometers the band gap is widened through an effect called quantum size confinement.[152] This allows for tuning the band gap in systems like nanoparticles[8,153] and thin films[154] to reach a compromise between light absorption efficiency and potential for photocatalyzed reactions. Band gap tuning by quantum size confinement is depicted in Figure 11. Very small dimensions also mean that the semiconductor does not have enough space to accommodate a space charge layer at low doping concentrations, making the bands essentially flat without applied bias. The lack of an electric field means that charge separation is entirely dependent on diffusion and might lead to increased recombination, despite the short distances the charge carriers need to travel.

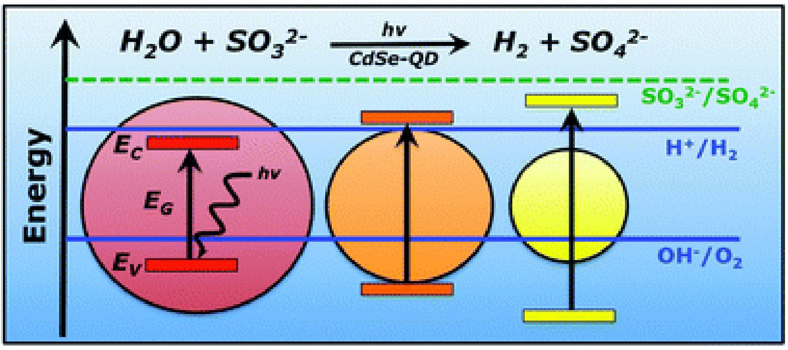

Figure 11. Schematic representation of band gap tuning of CdSe nanodots by quantum size confinement for photocatalytic water splitting. Republished with permission of The Royal Society of Chemistry, from [8], © 2012.

For thin film photoelectrodes, the thickness required for efficient light harvesting is in many cases larger than the optimum thickness for charge transport. In $BiVO_4$, for example, the charge carrier diffusion length is around 70 nm,[16] whereas the thickness required to collect 90 % of the incident light is close to 700 nm.[18] One way to decouple these factors is to prepare host-guest architectures, where porous transparent conductive oxides (TCOs) or other transparent conductive materials are used as scaffolds for photocatalytic thin film. For making these kinds of structures, where intimate contact between a nanostructured substrate and a thin film is required, ALD is an excellent choice. Bielinski et al.[19] used ALD to deposit $BiVO_4$ on ZnO nanowires and noticed 30 % increase in photocurrent as compared with flat films. Host-guest architectures also offer another way to increase the effective surface area of a photocatalyst.

Another consideration in manufacturing thin film nanostructures is that some materials, such as Fe_2O_3 and $BiVO_4$, have significantly lowered APCE when the film thickness is below a certain threshold.[27,155,156] The cause of this so-called "dead layer" effect is not entirely clear, but some proposed reasons are lattice mismatch between the film and the substrate and high defect concentrations at the interface.[27,155] Interfacial layers between the film and the substrate,[157] doping,[72] and deposition method of the film[18] can impact the thickness of the dead layer.

4.2 Semiconductor junctions

Single material photocatalysts, although simple, have several limitations that lower their efficiency. Firstly, the large band gap required in many cases lowers the light absorption efficiency. TiO_2, for example, has band edges well suited to catalyze both halves of the water splitting reaction, but its large band gap limits the absorption to the UV-spectrum. Secondly, in a single component semiconductor the charge separation is driven only by the space charge layer at the semiconductor/electrolyte interface.

One way to enhance charge separation is to form semiconductor homojunctions. They consist of layers of the same semiconductor with different dopants and doping levels and hence with different Fermi levels. For the system to reach an equilibrium, charge carriers diffuse towards areas with lower concentrations until the Fermi levels are equal. The resulting charge imbalance forms a space charge layer at the interface and creates an internal electric field that improves the charge separation (Figure 12).[21] Homojunctions are most often made from group IV semiconductors[132,138] because they are easier to dope both n- and p-type.[158]

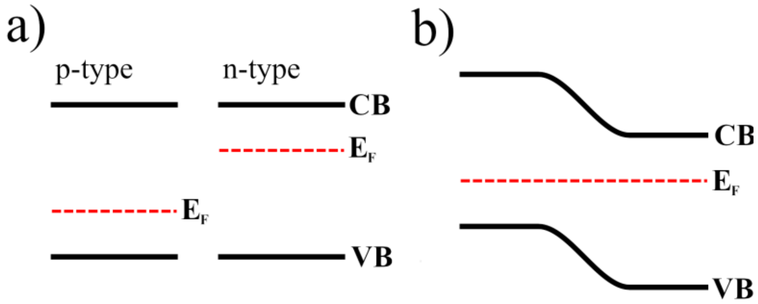

Figure 12. Energy band diagram of a semiconductor homojunction a) before contact and b) after contact.

Different semiconductors (demonstrated here with “SC 1” and “SC 2”) can be combined to form heterojunctions (Figure 13). Depending on the relative positions of the band edges, they can be classified to five different types and can offer more benefits than just better charge separation. Type I-1 and Type I-2 heterojunctions, collectively known as straddling gap heterojunctions, have both the valence and conduction band edges of SC-1 at more extreme potentials than those of SC-2. If the Fermi levels of SC-1 and SC-2 are similar then both holes and electrons are driven to the lower potentials of SC-2.[159–162] If the Fermi levels are different, the heterojunction has an internal electric field that promotes charge separation, like in the $TiO_2/BiVO_4$ nanocomposite synthesized by Zhang et al.[163] While one carrier is driven from SC-

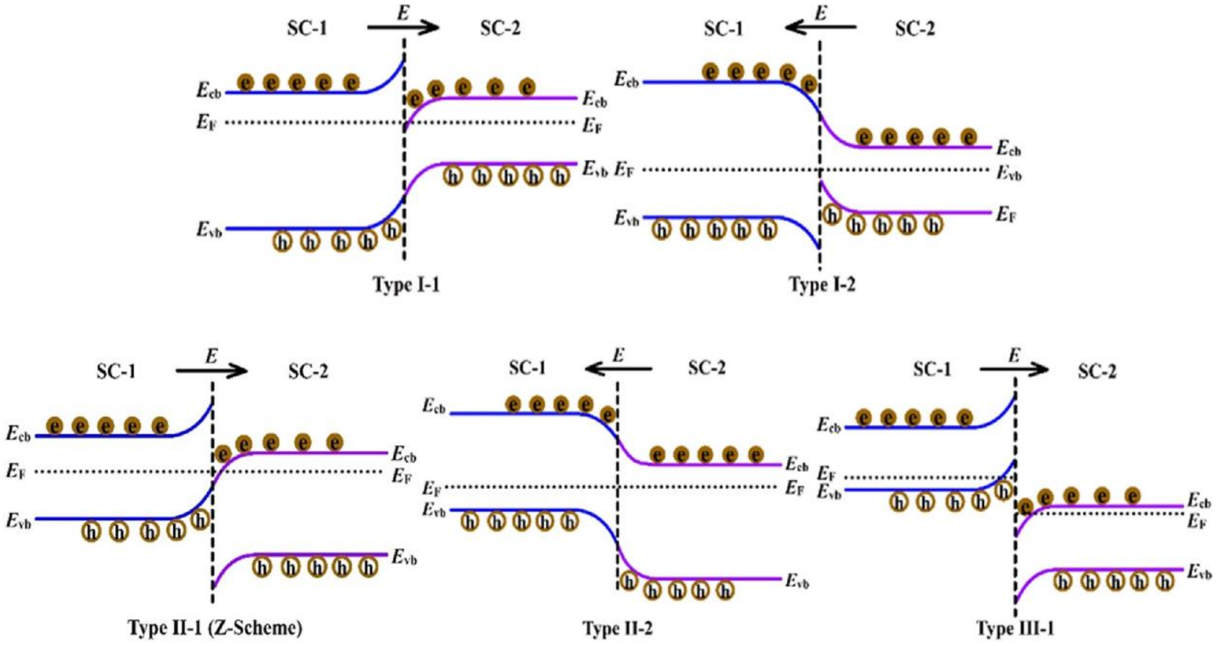

Figure 13. Band diagrams of various types of semiconductor heterojunctions. Reprinted from [18], © 2018, with permission from Elsevier.

1 to SC-2, the opposite carriers accumulate at the interface because they are unable to cross over to the higher potential band of SC-1. There is some concern that these trapped carriers increase the rate of recombination at the interface.[160] This kind of a heterojunction also has the disadvantage that the redox potentials are limited to those of the lower band gap semiconductor.

In a type II, or staggered gap heterojunction, both band edges of SC-1 are at higher level than the band edges of SC-2, but the valence band edge of SC-1 is still more positive than the conduction band edge of SC-2. If the Fermi level of SC-2 is higher than that of SC-1, the heterojunction is further classified as Type II-2. In this case an internal electric field forms that directs electrons to SC-2 and holes to SC-1, which enhances charge separation in both semiconductors[164] but lowers efficiency because charge carriers are transported to the semiconductors with smaller reduction and oxidation ability. Charge separation is also hampered by the coulombic repulsion of the charge carriers accumulating in the two semiconductors. An example of a Type II-2 heterojunction is the $BiVO_4/WO_3$ composite photoelectrode prepared by Hong et al.,[165] which showed photocurrent eight times greater than that of a bare $BiVO_4$ electrode. The improved performance was attributed to the complementary roles of the two light absorbers: $BiVO_4$ can absorb in a wider spectrum, whereas WO_3 has better conductivity.

On the other hand, if the Fermi level of SC-1 is higher than that of SC-2, a special type of junction called a Z-scheme (sometimes also called an S-scheme)[166] is formed (Type II-1 in Figure 13). Here the internal electric field directs both the photogenerated holes from SC-1 and electrons from SC-2 towards the interface, where they recombine. This accumulation of the opposite charges at the interface enhances charge separation through coulombic attraction. Some energy is lost in the recombination as heat or light, but it is compensated for by the fact that the remaining electrons and holes have higher redox potentials than those in type II-2 heterojunction. The higher potentials allow for much better oxidation and reduction capability with comparably narrow band gap materials.

The Z-scheme for photocatalysis was originally proposed by Allen Bard using two separate semiconductors in a suspension and a soluble redox pair that acted as an electron mediator between the two.[167] This approach is limited by the fact that it is difficult to stop the electron mediators from reacting with the higher potential bands,[168] leading to at least partial type II-2 behavior. Later research developed all solid-state Z-schemes with a metal layer as a mediator[169] that eliminates back reactions and the need for solution to carry the mediator, opening the possibility for also operating in gas phase systems. The mediator layers do, however, increase the complexity of the devices and typically require expensive noble metals. For this reason, direct Z-schemes as described above were eventually developed.[170,171]

An example of a $BiVO_4$ containing Z-scheme is the $BiVO_4/C/Cu_2O$ photocatalyst developed by Kim et al.,[172] where carbon acts as an electron mediator and as a barrier to protect the Cu_2O from photocorrosion. Photoluminescence intensity of a sample with $BiVO_4$ was greatly diminished as compared with C/Cu_2O or bare Cu_2O samples, indicating the formation of a heterojunction that inhibited the fast recombination of photogenerated charge carriers in Cu_2O. Accordingly, the photocatalytic CO_2 reduction rate (measured by rate of CO formation) with $BiVO_4$ in the photocatalyst was 3.3 times higher than with C/Cu_2O. $BiVO_4/C/Cu_2O$ was also the only catalyst that generated CH_4, in addition to CO. To study the charge transport pathway, Kim et al. monitored the oxidation of coumarin to 7-hydroxylcoumarin, which has a strong photoluminescence peak at 490 nm, whereas coumarin does not luminesce. As the valence band potential of Cu_2O is not positive enough for the oxidation reaction, it must take place by holes photogenerated in $BiVO_4$. This is depicted in Figure 14 along with the results that confirmed the Z-scheme charge transport.

Type-III, or broken gap heterojunction, consists of semiconductors that have no overlap of band gaps at all. According to some sources this configuration prevents charge transport from one semiconductor to another,[159,160] but others claim that the charge separation effect is akin to that of a type-II-2 heterojunctions but stronger.[161,162] The specific outcome is likely dependent on the direction of band bending at the interface. In any case, charge transfer between the semiconductors leads to such a great loss of potential that this is probably not an effective structure for increasing efficiency.

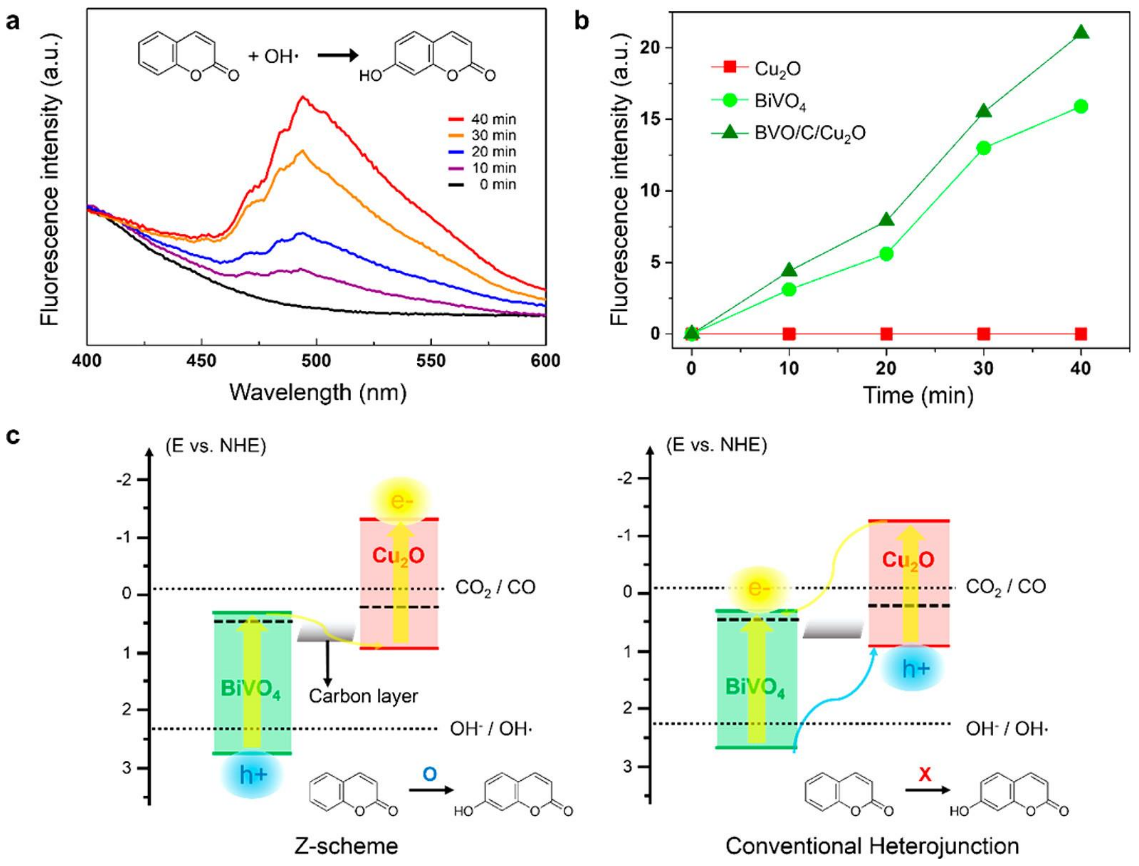

Figure 14. Oxidation of coumarin to verify the Z-scheme charge transport in $BiVO_4/C/Cu_2O$ photocatalyst as reported by Kim et al.: a) photoluminecence spectra of a coumarin solution with the photocatalyst after various intervals of illumination, b) fluorecence intensity of the solution as a function of illumination time for different photocatalysts, and c) energy band diagrams and charge transfer routes of Z-scheme and Type II-2 heterojunctions. Reprinted with permission from [172]. © 2018 American Chemical Society.

4.3 Doping

Doping of semiconductors refers to purposeful introduction of impurities into a material to modify its electrical properties. Dopants create either donor or acceptor states in the band gap and increase the density of electrons or holes, respectively. Shifting the balance of charge carriers can be used to create n- or p-type materials, and increasing the carrier density increases the conductivity.[21] The conduction type of many semiconductors used for photocatalysis is hard to change because of their extreme band edge positions. According to the doping limit rule, semiconductors with very positive valence band edges are difficult to dope p-type, and those with very negative conduction band edges are difficult to dope n-type.[158] Many photocatalytic materials still benefit from the increased conductivity, especially oxides such as Fe_2O_3.[173]

Besides modifying the conductivity of semiconductors, the acceptor and donor states in the band gap can widen the absorption spectrum because they allow absorption of photons with energy corresponding to the difference between the doping state and band edges (Figure 15). This kind of band gap engineering has been studied extensively in wide band gap oxides, such as TiO_2 and $SrTiO_3$.[89] In one example, the band gap of $La_2Ti_2O_7$ was narrowed from 3.8 eV to about 2.6 and 2.2 eV with Fe- and Cr-doping, respectively.[174] This extended the absorption to the visible spectrum, but the increased doping concentrations were also associated with lower photocatalytic activity due to faster recombination. TiO_2 and $SrTiO_3$ have also been codoped with Sb and Cr, which decreased the band gap energy to 2.2–2.4 eV.[175] Cr-doping alone led to a loss of the photocatalytic activity, but the addition of Sb partially remedied this. This was attributed to the Sb^{5+} ions maintaining charge balance with Cr^{3+} and suppressing the formation of Cr^{6+} ions that would act as recombination centers. The antimony doping alone did not have noticeable effect on the absorption.[175] A time-resolved IR absorption study showed that the codoping decreased the rate of electron hole recombination.[176]

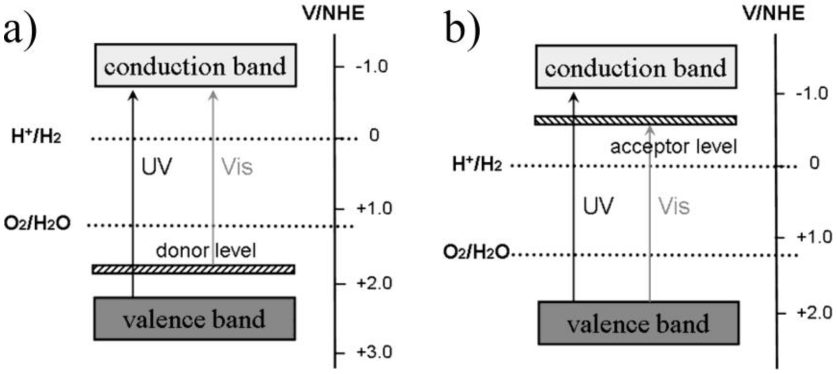

Figure 15. Energy band diagrams of semiconductors with a) donor levels and b) acceptor levels and their effect on light adsorption. Adapted with permission from [89]. Copyright 2010 American Chemical Society.

Whereas metal dopants generally form donor or acceptor states in the band gap, non-metal ions in oxides tend to shift the entire valence band edge to a less positive potential (Figure 16).[89] DFT calculations by Asahi et al.[177] showed that in the case of nitrogen and sulfur doping of TiO_2, the shift is caused by hybridization of the dopant anion 2p states with the O2p states. However, doping of TiO_2 with sulfur is presumed to be difficult because the S^{2-} ion is too large. Experimental measurements showed that N-doped TiO_2 indeed had a wider absorption spectrum and showed improved photocatalytic activity under visible light illumination.[177] Asahi et al. also theorized that, unlike the localized doping states of metal ions, the anionic doping states overlapping with the band edges are unlikely to form recombination centers. Contradicting this, Torres et al.[178] found that N-doped TiO_2 suffers from increased recombination due to trapping states, but they could not show conclusively if this is an intrinsic property of the material or related to defects such as surface states or poor crystallinity.

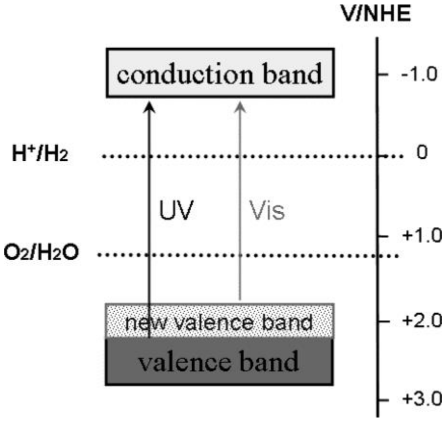

Figure 16. Energy band diagram showing the widening of the valence band by non-metal doping of semiconductors and the increased range of light absorption. Reprinted with permission from [89]. Copyright 2010 American Chemical Society.

Although the localized states of the metal ions act as trapping sites, the effect on photocatalysts is not necessarily detrimental. Trapping states are often associated with increased recombination,[174–176] but they also sometimes improve charge separation. Choi et al. studied doping of TiO_2 with 21 different metal ions.[179] They concluded that to increase the photocatalytic activity, a dopant should be able to trap both electrons and holes, which in turn would increase the carrier lifetimes. Trapping just one type of carrier leads to a faster recombination because the opposite charge carrier remains mobile and can quickly recombine with the trapped carrier. Additionally, the trapping states should lie close in energy to the bulk states to allow the trapped carrier to eventually migrate to the surface and react.[179] The studies on Cr/Sb codoped TiO_2[175,176] showed that although trapping both charge carriers might decrease the rate of recombination, it does not necessarily improve the photocatalytic activity. The main reason given for the diminished photocatalytic activity is that the trapping states decrease charge carrier mobility.

High dopant concentrations usually diminish the photocatalytic activity and beneficial effects peak generally somewhere below 10 at-% and often at as low as 0.5-1.0 at-% (compared to the total metal ion concentration).[173,174,180,181] Notably, these values are still much higher than those typically used in semiconductor electronics. The detrimental effect of excessive doping is usually attributed to either increased recombination[174,180] or decreased mobility of charge carriers,[181] which in turn increases recombination because fewer charge carriers reach the surface. The increased charge carrier concentration from doping also makes the space charge layer narrower at the photocatalyst interfaces.[23] This means that fewer charge carriers are generated directly in the space charge layer, where they are most efficiently separated. In nanostructures with feature sizes too small to accommodate the space charge layer of an undoped semiconductor, the narrower space charge layer might be beneficial, however.

For $BiVO_4$, the most common dopants are tungsten[16,182,183] and molybdenum.[184,185] Park et al.[61] conducted a systematic study of codoping drop-casted $BiVO_4$ with these two elements and found that the highest photocurrent was obtained with a combination of 2 at-% W and 6 at-% Mo. An associated DFT study attributed the increased photocatalytic activity of doped $BiVO_4$ to an enhancement of charge carrier mobility via higher carrier density.[61] Other studies have found that W-doping increases the number of electron traps and decreases carrier mobility and lifetime but also increases carrier density,[16] or that it decreases the number of hole traps and thus increases carrier lifetimes.[183] Both of the latter hypotheses are also supported by experimental evidence, and so the mechanism by which W-doping improves the photocatalytic performance of $BiVO_4$ remains unresolved.

Abdi et al. used a spray pyrolysis method to deposit a stepped gradient homojunction of $BiVO_4$ where W doping was rising from 0 to 1 at-% along the film thickness.[182] Schematic of the band structure of this gradient junction is presented in Figure 17d. Carrier separation efficiency at 1.23 V vs. reversible hydrogen electrode (RHE) was reported to increase by 22 % in comparison to a homogeneously doped film. Some other dopants that have been studied in $BiVO_4$ include lanthanides La, Ce, Sm, and Yb, of which the latter two improved the photocatalytic activity.[186] A series of 12 metal ions (Mo, W, Ti, Cr, Fe, Zn, Nb, Ru, Pt, Sn, Ce, and Ta) were studied by Parmar et al.,[29] but only Mo and W were beneficial. Only nitrogen has been investigated for anionic doping of $BiVO_4$. It both decreased the band gap width and improved charge separation.[187] Unfortunately the N-doping also decreased the stability of the NiOOH/FeOOH cocatalyst on the $BiVO_4$, and loss of the cocatalyst after 30 h of operation was reported.

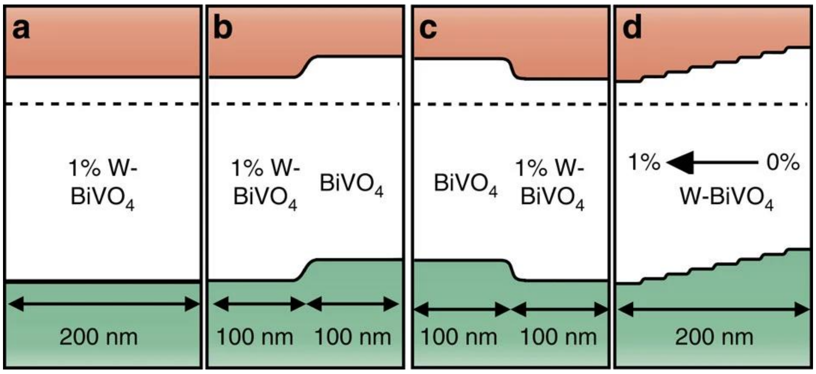

Figure 17. Energy band diagrams of a) homogeneously doped $BiVO_4$, b) W-doped/undoped $BiVO_4$ homojunction, c) reverse homojunction and d) a 10-step gradient homojunction. Reprinted by permission from Springer Nature: [182], © 2013.

Although not fitting the exact definition of doping, nonstoichiometry of Bi and V was also observed to affect the photocatalytic performance of $BiVO_4$. Berglund et al.[188] reported that films with excess vanadium (V:Bi atomic ratio of 2) deposited with reactive ballistic deposition were photocatalytically more active than stoichiometric ones, which was proposed to be due to improved surface reaction kinetics. Part of the excess vanadium dissolved into the electrolyte during operation, and the photocurrents decreased by 70 % during 3 h of operation, after which they stabilized. Anyhow, even after this decrease the photocurrents of the films with excess vanadium remained higher than those of the stoichiometric films. Interestingly, despite the large excess of vanadium, no additional phases were observed.[188]

4.4 Cocatalysts and interfacial layers

In addition to being used for heterojunctions, additional materials can also be used in interfacial layers for a variety of reasons, such as passivation layers to protect the semiconductor against photocorrosion, underlayers to enhance charge transport, and hole or electron blocking layers to prevent recombination. These can also be thought of as an extension to the semiconductor-semiconductor heterojunctions, as the interfacial layers can also contain metals and insulators. In many cases they might be like the previously described heterojunctions and benefit from the band bending effects, but the specialized uses warrant the inspection of interfacial layers as a separate group. In the same vein, cocatalysts also form a heterojunction, but the primary purpose for their use is to enhance the reaction kinetics at the photocatalyst surface. However, cocatalysts can also fill the role of the other interfacial layers in many cases.

Although photocatalysts are used to power chemical reactions, their surfaces might be poorly suited for redox reactions. Some light absorber materials are, in fact, inactive towards certain reactions without some kind of a cocatalyst.[113] Even with intrinsically active photocatalysts, the addition of a cocatalyst can tremendously increase the efficiency.[59] Often materials that have previously been studied as electrocatalysts are used as cocatalysts. They work by lowering activation energies of the redox reactions and so increase the efficiency through kinetic factors. Zachäus et al.[59] also proposed two additional roles for a cocatalyst: to passivate the photocatalyst surface to prevent surface recombination, and to enhance charge transport through band bending at the surface. Principles of passivating and non-passivating cocatalysts are demonstrated in Figure 18.

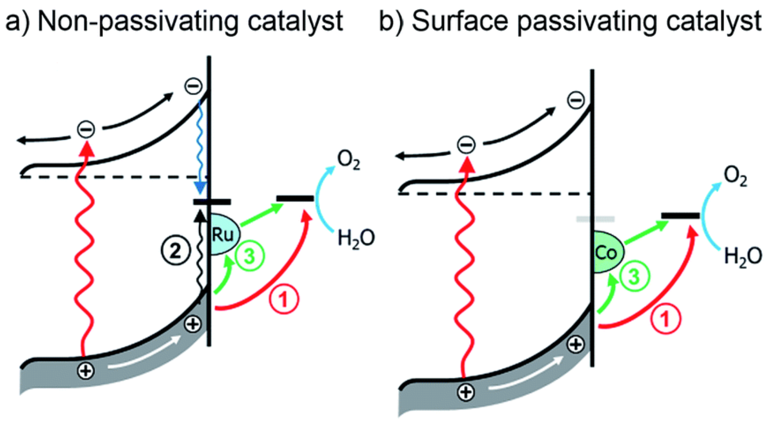
a) Non-passivating catalyst b) Surface passivating catalyst

Figure 18. Effects of surface passivating and non-passivating cocatalysts. Photogenerated charge carriers in semiconductors with the non-passivating cocatalysts can take part in redox reactions directly at the semiconductor surface (1), recombine at the surface (2), or transfer to the cocatalyst and react (3). With the passivating cocatalysts only routes (1) and (3) are available. Adapted from [59] under Creative Commons: CC BY-NC 3.0.

Noble metals are commonly used as cocatalysts for their electronic properties. Platinum, for example, has been used as a reduction cocatalyst with many semiconductors.[189,190] Aside from the high price, a difficulty with many noble metals as cocatalysts for the water splitting is that they also catalyze the reduction of O_2 back to water. Maeda et al.[33] introduced a way to prevent the back reaction by depositing Rh/Cr_2O_3 core/shell nanoparticles as the cocatalyst. The Cr_2O_3 shell can catalyze the hydrogen evolution reaction while the Rh core aids in electron extraction from the photocatalyst, but the Cr_2O_3 shell is not active towards the reduction of O_2.[33] Some more economical hydrogen evolution catalysts include nanoparticulate MoS_2[191] and the transition metal phosphides NiP_2 and Co_2P.[192,193]

Common cocatalysts for oxidation reactions are IrO_2[194] and RuO_2,[113] but more earth-abundant cocatalysts have been developed for this application as well. One that is used often is Co-Pi,[195] which is a rather poorly defined amorphous mixture of cobalt phosphates and oxides electrodeposited from a Co^{2+} containing potassium phosphate buffer solution. It shows improvement of the photocatalytic activity for many oxygen generating photocatalysts.[59,196] Risch et al.[197] attributed the high activity to a metal-oxo structure analogous to the Mn complex in the photocatalytic enzyme of plants, photosystem II.[198] Photochemical deposition of Co-Pi has also been demonstrated and was claimed to make a better contact with the hole-accumulating surface sites of a semiconductor.[30] Oxygen evolution cocatalysts used with $BiVO_4$, in addition to those mentioned previously, include photodeposited NiOOH/FeOOH double layer[199] and metallic bismuth.[200]

Based on intensity modulated photocurrent spectroscopy, Zachäus et al.[59] made a convincing argument that the main limiting factor of $BiVO_4$ in photocatalysis is fast surface recombination, rather than poor water oxidation kinetics as is often claimed. They suggested that Co-Pi at least passivates the surface defects that would otherwise promote recombination. One experiment that showed how important even minor surface modifications can be for photocatalytic activity was the deposition of TiO_2 thin films with ALD on commercially available TiO_2 photocatalyst powder by Trochowski et al.,[9] even though the effect was not beneficial in all cases. Al_2O_3, on the other hand, has been shown to efficiently passivate surface trapping states on Fe_2O_3,[198] TiO_2,[201,202] and $BiVO_4$.[203] Eisenberg et al.[204] used selective electrodeposition of TiO_2 on a discontinuous $BiVO_4$ photoanode to simultaneously passivate exposed conductor surfaces against back reactions and $BiVO_4$ surface defects to prevent recombination.

As discussed above, many photocatalysts are vulnerable to photocorrosion and degradation upon illumination. One way to make the photocatalysts more robust is to deposit a passivating layer on the surface. This task is made challenging by the fact that the layer itself needs to be resistant to corrosion while also being able to transport the photogenerated charge carriers and catalyze redox reactions. Therefore, the protective layer is often formed by making a continuous cocatalyst layer, but dedicated protective layers have also been demonstrated. Stability and compatibility of the cocatalysts also need to be considered, as demonstrated with N-doped $BiVO_4$: the FeOOH/NiOOH, which was previously shown to be stable on unmodified $BiVO_4$,[199] was partially lost after only 30 h of operation when deposited on N-doped $BiVO_4$.[187]

Noble metals are good cocatalysts for many reactions, and they are also highly resistant to corrosion. For this reason, and for the excellent charge transport due to their conductivity, they are often used as protective layers.[189,205,206] A p-silicon photoanode covered with a platinum film showed stable photocurrent for 60 days of operation.[205] Similarly, a 10 nm film of platinum deposited with ALD allowed a CdSe photoanode to preserve 80 % of its initial photocurrent after 6 h of operation in acidic electrolyte. In comparison, just 8 % of the photocurrent was retained without the protective layer.[189] A nickel coated n-Si photocathode, in turn, showed stable O_2 generation for 80 h in an aqueous K-borate/Li-borate electrolyte.[206] The downside of metallic protective layers is their reflectivity, which makes light absorption less efficient.[189]

Metal oxides, on the other hand, are often transparent and very stable in various electrolytes. TiO_2 layers have been used as protective layers in acidic and basic conditions for both photoanodes and photocathodes. However, the conductivity of metal oxides is often not very good, and charge transport across the protective layer relies on various mechanisms. In n-type oxides the conduction band edge is often at low enough level so that electrons can migrate through the conduction band. Other mechanisms have been proposed to explain the hole conductivity through different protective layers. These hole transport mechanisms are depicted in Figure 19.

In short, the holes can conduct through the protective layer if it is p-type[207] or through defect states in the band gap of an n-type oxide. The latter was demonstrated by Hu et al. with an amorphous conductive TiO_2 deposited with ALD.[208] The selection of p-type oxides is quite limited, however. Insulating oxides may also be used when the layer is made thin enough to enable tunneling through it,[209,210] but making films thin enough while retaining complete coverage of the semiconductor poses a challenge.[211] Yet another transport mechanism with n-type protective oxides is injection of electrons from the cocatalyst inwards through the conduction band of the protective layer to recombine with the photogenerated holes at the interface.[212]

Although not damaging for the photocatalysts like photocorrosion, recombination of electron-hole pairs at interfaces causes significant loss of efficiency. Some cocatalysts passivate the recombination-causing surface defects, but layers that enhance charge transport and decrease recombination at the various solid interfaces have been developed as well. Interfacial layers

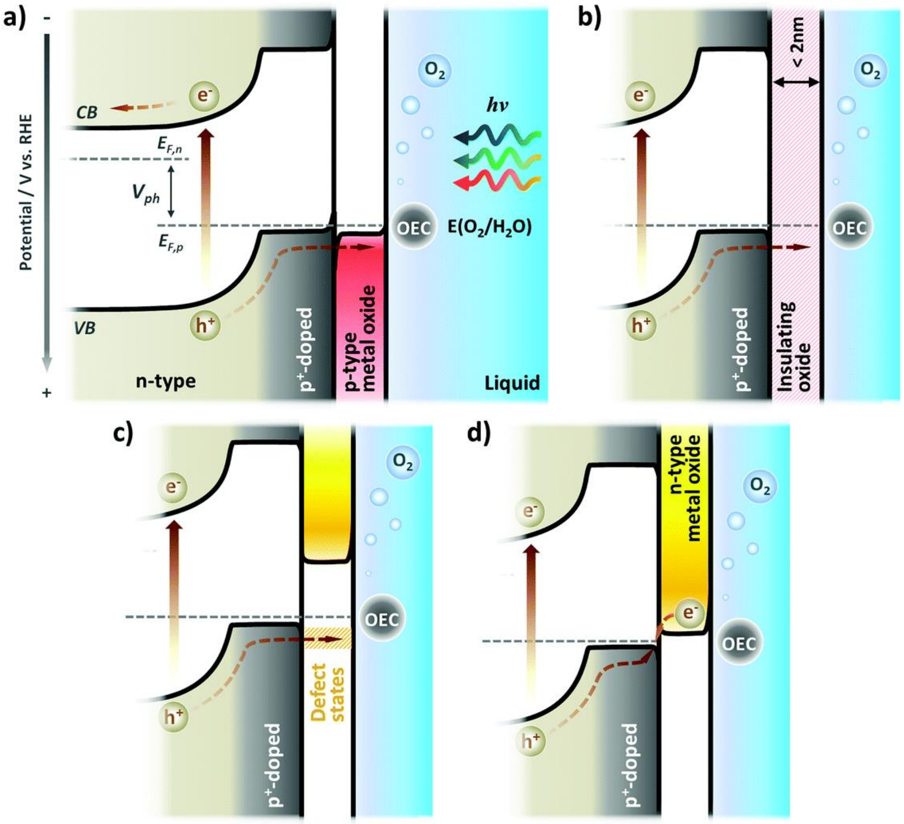

Figure 19. Hole transport mechanisms in protective metal oxide layers for buried junction photocatalysts: a) hole conduction in p-type protective oxide, b) tunneling, c) hole transport through defect states and d) recombination with electron from a cocatalyst through the conduction band of an n-type protective oxide. Oxygen evolution catalyst is abbreviated as OEC. Used with permission of Royal Society of Chemistry, from [271]; permission conveyed through Copyright Clearance Center, Inc.

between the semiconductor and the conductor in photoelectrodes have been shown to be beneficial,[213] and in α-Fe_2O_3 photoanodes they are especially significant, as they can help to eliminate the dead layer effect.[157] The benefit of defect passivation has been demonstrated even at the semiconductor/protection layer interface[214] with a TiO_x layer that decreased the number of donor-like defects at the n-Si/ITO interface.

Interfacial layers that promote charge transport have also been developed. CdS and ZnO, for example, have been used to enhance charge transport to a protective TiO_2 layer by essentially forming a series of type-II-2 heterojunctions (Figure 13).[215] Interlayers with suitably positioned band edges can also be used to form hole or electron blocking layers that enhance charge separation and prevent recombination at the semiconductor/conductor interface.[148,216] An example of such a layer is a SnO_2 layer that prevents holes from reaching the back contact of the photoanode but allows electrons to pass (Figure 20).

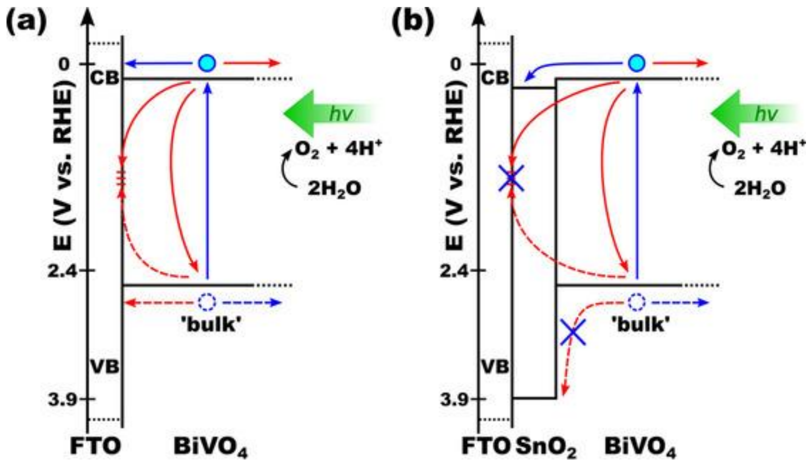

Figure 20. Energy band diagram showing the effect of SnO_2 interlayer on recombination at $BiVO_4$-conductor interface. Reproduced with permission from [148], © 2019 Wiley-VCH Verlag GmbH & Co. KGaA, Weinheim.

5 Atomic Layer Deposition of Bismuth Vanadate

5.1 Binary oxide processes

The simplest way to deposit ternary oxides, such as $BiVO_4$, with atomic layer deposition is to combine two binary oxide processes. For both bismuth and vanadium, multiple ALD-precursors exist, and many of them have been used with both conventional oxygen sources, H_2O and O_3. O_2-plasma has also been employed in some cases. Tables 4 and 5 summarize bismuth and vanadium precursors, respectively, used so far in binary or ternary ALD processes, along with relevant growth parameters.

Table 4. Bi precursors used in literature for Bi_2O_3 or ternary bismuth oxide depositions.

Bi Precursor	Evaporation temperature (°C)	Oxygen precursor	Deposition temperature (°C)	Growth per cycle (Å)	Source
$Bi(dmb)_3$	60–85	H_2O	140–150	0.3–0.38	[19,217–220]
$Bi(mmp)_3$	135–145	O_3	200–290	0.40	[221,222]
$Bi(N(SiMe_3)_2)_3$	110–130	H_2O	190–200	0.15–0.23	[223]
$Bi(O_2C^tBu)_3$	not reported	H_2O	300	0.06	[217]
$BiPh_3$	130	H_2O	130	0.10	[17,18]
$BiPh_3$	115–200	O_3	250–320	0.23–0.40	[222,224]
$Bi(thd)_3$	140–200	H_2O	190–300	0.07–0.45	[225–231]
$Bi(thd)_3$	190	O_2-plasma	280–330	0.35	[229]

dmb=2,3-dimethyl-2-butoxide, mmp=1-methoxy-2-methyl-2-propoxide, Me=methyl, ^{t}Bu=tert-butyl, Ph=phenyl, thd=2,2,6,6-tetramethyl-3,5-heptanedionate.

As can be seen, Bi_2O_3 processes generally have rather low growth per cycle (GPC) values. Deposition temperatures are moderate to low compared with most oxide ALD processes.[13] At temperatures of 150–200 °C the thermal processes result in amorphous Bi_2O_3.[217,223,224,229,231] The low GPC values reported for the $Bi(thd)_3$+H_2O process have been attributed to the large thd ligands, low reactivity, and incomplete reactions during the H_2O pulse. Impurities also pose a problem: Müller et al.[229] reported up to 9.5 at-% carbon in the films grown with $Bi(thd)_3$ and H_2O. For $Bi(O_2C^tBu)_3$, Hatanpää et al.[217] speculated that a stronger oxidizer than water is needed to increase GPC.[223] The $Bi(N(SiMe_3)_2)_3$-H_2O process was reported to be difficult to repeat.[223] $BiCl_3$ has also been investigated as a precursor, but it resulted in BiOCl films.[232]

Table 5. Vanadium precursors reported for deposition of VO_x thin films.

V Precursor	Evaporation temperature (°C)	Oxygen precursor	Deposition temperature (°C)	GPC (Å)	Source
TDMAV	25–40	H_2O	50–135	0.30–0.40	[234–237]
TDMAV	25	O_3	50–120	0.45	[234]
TEMAV	65–70	H_2O	125–200	0.67–0.80	[238–240]
TEMAV	65–70	O_3	100–175	0.31–1,05	[238–240]
$V(amd)_3$	190	H_2O	200	1.57	[241]
$V(amd)_3$	190	H_2O_2	200	0.38	[241]
$V(amd)_3$	190	H_2O/O_2	200	0.41	[241]
VCl_4	30	H_2O	350	0.30	[242]
$VO(acac)_2$	140	O_2-plasma	200	0.45	[243]
$VO(thd)_2$	125	O_3	215	0.45	[244]
VTIP	25–55	H_2O	60–230	0.20–1.00	[245–252]
VTIP	40–45	O_3	170–185	0.28–0.81	[253–255]
VTNP	45	H_2O	170–190	1.00	[256]

TDMAV=tetrakis(dimethylamido)vanadium, TEMAV=tetrakis(ethylmethylamido)vanadium, amd=diisopropylacetamidinate, acac=acetylacetonate, thd=2,2,6,6-tetramethyl-3,5-heptanedionate, VTIP=vanadium triisopropoxide oxide, VTNP=vanadium tri-n-propoxide oxide.

For the most part, VO_x processes have much lower deposition temperatures than the Bi_2O_3 processes, with correspondingly low vanadium precursor decomposition temperatures. VTIP, for example, starts decomposing above 90 °C already.[249] The CVD-type growth arising from the decomposition is so slow, however, that many studies report much higher upper limits for the ALD-window. [245–248,250–255] Vanadium has many stable oxidation states, which is reflected in the different precursors. Consequently, when using V(+3) or V(+4) precursors, the oxidation of vanadium to the +5 state is not certain even with O_3,[257] and post-deposition processing steps might be needed to ensure the +5 oxidation state. For a more in-depth account of VO_x processes, Prasadam and coworker's 2019 review[258] is recommended.

Deposition temperatures of selected Bi_2O_3 and VO_x processes are compared in Figure 21. As can be seen, there is sufficient overlap to combine most of the processes despite the general difference in ALD-windows. Furthermore, precursor reactivity in ternary processes often

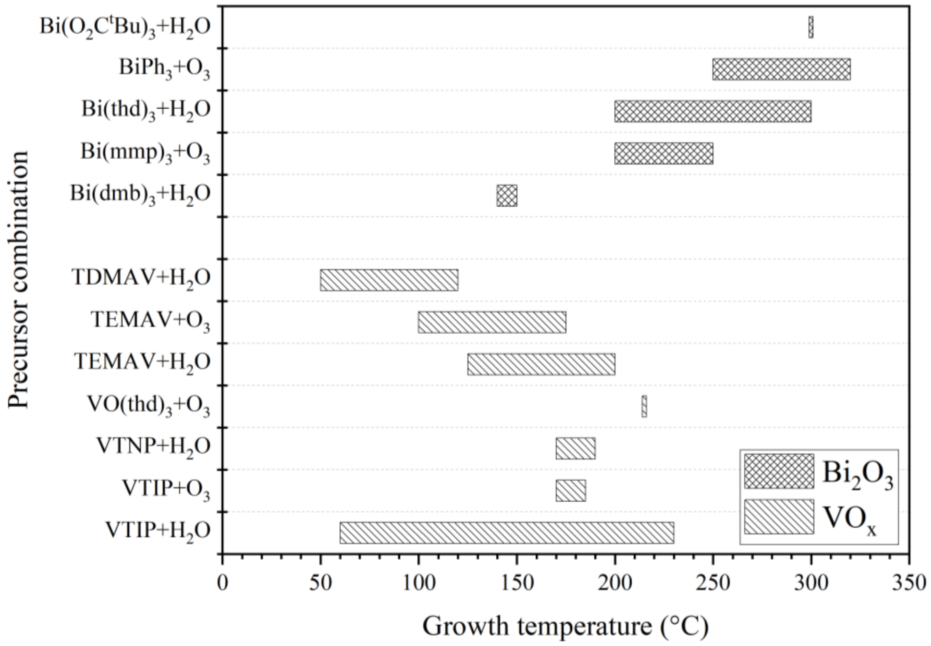

Figure 21. Comparison of deposition temperatures of different precursors for Bi_2O_3 and VO_x.

differs from the binary ones. A good example of this variability is the VTIP-$BiPh_3$-H_2O process,[17] which will be discussed shortly. Bismuth oxide also reduces to metallic bismuth in some ternary ALD processes, which further complicates the chemistry.[259]

5.2 $BiVO_4$ processes

To date, three ALD processes for depositing $BiVO_4$ have been reported.[17–19] The earliest process, reported by Morgan Stefik, used supercycles consisting of consecutive VTIP-H_2O and $BiPh_3$-H_2O cycles at a deposition temperature of 130 °C.[17] $BiPh_3$ by itself does not react with water in ALD, but in ternary processes such as this, and the Bi-Ti-O process with $BiPh_3$, $Ti(O^iPr)_4$, and water by Schuisky et al,[259] the $BiPh_3$-H_2O combination does result in deposition of ternary oxides of bismuth. The different reactivity is attributed to a catalyzing effect of the other oxide. Indeed, when the number of $BiPh_3$+H_2O cycles was increased in Stefik's process, the Bi content did not increase in the same proportion. With one $BiPh_3$ pulse and one VTIP pulse the V:Bi atomic ratio was 2.01, whereas doubling the number of $BiPh_3$ cycles resulted in a ratio of 1.87. This is further evidence of the catalyzing need of the catalyzing effect for bismuth oxide deposition with $BiPh_3$ and H_2O. Stefik also noted that leaving out the water pulse after either the $BiPh_3$ or the VTIP pulse results in very low Bi content of around 1 at-%.

Because of the low reactivity, $BiPh_3$ is not suitable for depositing stoichiometric $BiVO_4$ with VTIP and water. To make stoichiometric $BiVO_4$, Stefik annealed the films at 450 °C which caused the excess vanadium to precipitate out as V_2O_5, and then etched the films in 1 M NaOH to selectively remove the V_2O_5. This treatment creates an island-like morphology with areas of $BiVO_4$ separated by large voids where the V_2O_5 was etched away. This morphology might affect the photocatalytic efficiency by increasing the catalytic surface area but also conversely by increasing the density of carrier trapping sites on the surface.

Another way to enhance the stoichiometry is to tune the stoichiometry of the as-deposited films. Lamm et al.[18] approached the problem by limiting the growth of V_2O_5 instead of trying to increase the number of $BiPh_3$+H_2O cycles. This inhibition of growth was achieved by modifying the previous process: a pulse of an alcohol was used to block reaction sites before the VTIP pulse, attenuating the deposition of V_2O_5. Methanol, ethanol, and 2-propanol were compared, and the inhibiting effect on the V_2O_5 deposition was the greatest for methanol and the smallest for ethanol with isopropanol in between. In the $BiVO_4$ deposition the process utilizing methanol resulted in a stoichiometry closest to that of $BiVO_4$: the atomic ratio of V to Bi was 1.18. Curiously, the GPC of the process remained roughly the same, 0.075 Å, compared to the 0.070 Å of the unmodified process.[17,18] Lamm et al. proposed that this is caused by spatial distribution of V-OH surface sites along with steric effects that enhance the catalytic effect on $BiPh_3$.

The third process, developed by Bielinski et al.,[19] uses $Bi(dmb)_3$ and VTIP as the metal precursors at a deposition temperature of 150 °C. Using a more reactive Bi precursor allows the deposition of Bi_2O_3-V_2O_5 nanolaminates that are then annealed to form the $BiVO_4$. Adjusting the layer thicknesses in the nanolaminate makes it possible to control the film composition rationally. The nanolaminate approach also mitigates the strong nucleation effect observed for the Bi_2O_3 deposition on V_2O_5 with $Bi(dmb)_3$. Linear GPC values of Bi_2O_3 and V_2O_5 were 0.30 Å and 0.48 Å, respectively. The thicknesses of individual layers were 6–12 nm, but after annealing at 450 °C the films showed no composition gradients. Elemental mapping of the film cross sections was done in scanning transmission electron microscope (STEM) with energy dispersive X-ray spectroscopy (EDS). Stoichiometry closest to 1:1 as in $BiVO_4$ was achieved by depositing Bi_2O_3 and V_2O_5 in a cycle ratio of 270:230. The V-rich films deposited with 250:250 Bi_2O_3 to V_2O_5 cycle ratio exhibited segregation of a V_2O_5 phase when annealed. By contrast, Bi-rich films did not show evidence of Bi_2O_3 or Bi-rich vanadate phases in grazing incidence x-ray diffraction.[19]

All the aforementioned publications evaluated the optical properties and photoelectrocatalytic performance of films grown on fluorine doped tin oxide (FTO) glass. Indirect band gaps of the films grown by Stefik were 2.28 eV before the excess V_2O_5 was etched and 2.24 eV after.[17] The direct band gaps were 2.64 and 2.58 eV for the unetched and etched films, respectively.[17] Flat band potential was reported to be around 0 V vs. RHE.[17] The films grown by Bielinski et al.[19] had a band gap of about 2.5 eV, with a slight increase associated with a larger Bi content. These values correspond well to the band gap of bulk $BiVO_4$, which is reported to be 2.5 eV.[7]

For measuring photoelectrode performance, simulated AM 1.5 spectrum light was used in all three studies. Solutions with sulfite ions as hole scavengers were also used to ensure quantitative charge carrier injection from the catalyst to the electrolyte, thus allowing the measurement of photoanode performance without the use of cocatalysts. The reported photocurrent densities are gathered in Table 6. Stefik found that the photocurrent density was lower for the etched films.[17] The decrease was attributed to inadvertent loss of some $BiVO_4$¸ as light absorption was also weaker. Light harvesting efficiencies of the unetched and etched films were 56.7 % and 44.8 %, respectively, calculated as a percentage of the full absorption of the AM 1.5 spectrum up to 2.4 eV.[17] Charge carrier separation efficiency of both films was 28 %. Stefik noted that the charge separation is the major limiting factor in thin films.

Lamm et al.[18] studied the effect of film thickness on photocatalytic performance and demonstrated that the films start being limited by charge transport instead of charge separation between 60 and 75 nm of thickness. This was as expected, as charge carrier diffusion length in $BiVO_4$ is around 70 nm.[16] However, the photocurrent density still increased monotonically as a function of the film thickness and was the highest for the 75 nm film. Another interesting finding in this study was that the so-called dead layer effect, where films do not exhibit any photocatalytic activity below a certain thickness, ended at much lower thickness with the ALD grown $BiVO_4$ films as compared with films grown with other methods. For the ALD grown $BiVO_4$ the dead layer thickness was only 7.5 nm, whereas films deposited by spray pyrolysis were found to have a dead layer as thick as 50 nm.[27]

Table 6. Reported photocurrent densities for different ALD-$BiVO_4$ photoanodes. All samples in the 2017 study by Lamm et al. were annealed and etched after the deposition. The cycles in the sample information for Bielinski et al. refers to the ratio of Bi_2O_3 cycles to V_2O_5 cycles. Samples were grown on FTO unless stated otherwise and illuminated by AM 1.5 spectrum light in buffered sulfite solution.

Study/source	Sample information	Photocurrent density (mA/cm^2) at 0.60 V vs. RHE	Photocurrent density (mA/cm^2) at 1.23 V vs. RHE
Stefik[17] ($BiPh_3$ + VTIP + H_2O)	55.6 nm film, annealed	0.73	1.15
	55.6 nm film, annealed & etched	0.62	0.95
Lamm et al.[18] ($BiPh_3$ + CH_3OH + VTIP + H_2O)	7.5 nm film	0.10	0.04
	15 nm film	0.08	0.22
	22.5 nm film	0.14	0.34
	30 nm film	0.35	0.70
	45 nm film	0.30	0.67
	60 nm film	0.42	0.81
	75 nm film	0.69	1.21
Bielinski et al.[19] ($Bi(dmb)_3$ + VTIP + H_2O)	250:250 cycles 40 nm film		2.16
	270:230 cycles 40 nm film		2.24
	290:210 cycles 40 nm film		2.03
	$BiVO_4$ on ZnO nanowires		2.9

Bielinski et al.[19] reported significantly larger photocurrent density than either of the previous studies. The improvement is in part because they had a 3 nm hole blocking interlayer of SnO_2 in between the FTO electrode and $BiVO_4$, which improves the charge separation efficiency. This effect was minor, however, and most of the improvement over the other samples can likely be attributed to the film quality. It is possible, for example, that the etching steps in the other studies result in a higher density of surface recombination sites. The film closest in stoichiometry to $BiVO_4$ exhibited the highest photocurrent density among the planar electrodes. A nanostructured photoelectrode was also fabricated, comprising $BiVO_4$ on ZnO nanowires with a SnO_2 interlayer. The photocurrent density was 30 % higher than that of a planar electrode at 1.23 V vs. RHE.

Lamm et al.[148] have also conducted a study on the effect of ALD grown SnO_2 interlayers on ALD-$BiVO_4$/FTO planar electrodes and ALD-$BiVO_4$/antimony doped tin oxide (ATO) nanotube electrodes. The best performance was achieved with an 8 nm interlayer.[148] Thinner layers were speculated to have pinholes caused by island growth or crystallization procedures, or to suffer from diffusion of fluorine into the interlayer. Thicker layers were assumed to decrease the efficiency by increasing the ohmic resistance of the anodes. With 2.2 µm long ATO nanotubes as the substrate, the optical thickness of the electrode was greatly increased, resulting in a photocurrent value of 2.1 mA/cm^2 at 1.23 V vs. RHE, which is more than three times the value achieved with the corresponding planar electrode.[148]

Although $BiVO_4$ is often reported to be a very stable photocatalyst, all these studies evidenced some loss of performance during the operation. Stefik reported 20 % smaller photocurrent density after 2 h, whereas Bielinski et al.[19] reported a comparable figure of 26 %. Lamm et al.,[18] however, reported that during the first 1 h of operation the photocatalytic performance increased drastically, and then dropped by just 11 % during 17 h of operation. On the basis of this observation, they devised a photoelectrocatalytic activation treatment and investigated the samples with x-ray photoelectron spectroscopy (XPS). The results revealed that right after the annealing the films have minor components of Bi^0 and V^{4+}, but these reduced states are absent in the activated films. As Lamm et al. pointed out,[18] specific defect chemistry resulting from the synthesis method has a strong influence on the photocatalytic performance.

6 Summary

This literature study gave an overview of how light-induced charge carriers in semiconductors can be used to power chemical reactions. The main way to improve the efficiency of photocatalysis is to enhance the light absorption and charge transport in semiconductors while preventing recombination of charge carriers and back-reaction of the products. These processes are mostly affected by the inherent properties of the semiconductor material, but various strategies can be employed to modify and otherwise improve the materials.

Generalizing semiconductor properties on the basis of chemical composition alone can be misleading because structural factors also greatly affect the electronic properties. It can be said, however, that most non-oxide semiconductors are rather unstable in aqueous photocatalysis. On the other hand, most oxides are quite stable but have valence band edges at very positive potentials. Consequently, low band gap oxides with high conduction band edges are rare, which means that making stable photocatalysts with both good reduction and oxidation potential is difficult. One way to shift the valence band edge of oxides to less positive values is to incorporate bismuth into the structure. $BiVO_4$, as a Bi-containing n-type oxide, strikes a good balance of properties for photocatalytic water oxidation, and its main efficiency limiting factor is surface recombination of charge carriers.

Limitations of different materials can be overcome with various modifications, if the added manufacturing complexity can be justified for a given application. Nanostructuring, semiconductor junctions, and doping can improve the charge transport and light harvesting properties of semiconductors, whereas cocatalysts improve surface reaction rates, and protective layers prevent photocorrosion. Rational design of photocatalytic structures is still rather difficult, as the operating principles of many efficiency improving techniques are still under debate. Regardless, many of these modifications benefit from thin film deposition techniques. ALD especially is very well suited for fabricating nanostructured and doped photoelectrodes and thin but continuous interlayers.

Literature on ALD of $BiVO_4$ was studied in detail, and it seems that the best photocatalytic performance can be achieved with annealed nanolaminates. This advantage is probably due to the avoidance of an etching step that the other processes use to dissolve excess V_2O_5. The lack of this additional step also makes the deposition process itself more streamlined. Deposition of the ALD-$BiVO_4$ films on nanostructures has also been demonstrated and was found to improve the photocatalytic performance. These processes still leave room for improvement, and development of new ones can very well turn out beneficial, which is why the binary ALD processes for Bi_2O_3 and VO_x were also catalogued. On the basis of that survey, $Bi(dmb)_3$ and TEMAV were determined to be a good combination of precursors for their compatible deposition temperatures and availability. The following experimental part of this thesis details the development of a new ALD $BiVO_4$ process based on these precursors.

7 Experimental methods

7.1 Film deposition

ALD depositions were carried out in an ASM Microchemistry F-120 cross-flow hot wall ALD reactor in a pressure of 2-5 mbar. The precursors used were bismuth(III) 2,3-dimethyl-2-butoxide ($Bi(dmb)_3$, synthesized in-house) for Bi_2O_3 and tetrakis(ethylmethylamido)-vanadium(IV) (TEMAV, supplied by Air Liquide, purity assay 99,49 %) for VO_x. $Bi(dmb)_3$ and TEMAV were evaporated from glass boats inside the reactor at temperatures of 85 and 40–65 °C, respectively. The precursors were handled in a glove box and transported to the reactor in glass boats sealed with laboratory film (Parafilm). Deionized water from an external container was used as the oxygen precursor, and its flow was controlled by a needle valve. Nitrogen (99.999 % purity) was used as a carrier and a purging gas.

Films were deposited on Si(100) substrates with the native oxide and for UV-vis spectrometry measurements on Si(100) and soda-lime glass substrates passivated with an Al_2O_3 ALD coating deposited in situ from TMA and water. The soda-lime glass substrates were cleaned before deposition with an ultrasonic cleaner in water with ultrasonic detergent (Branson, Emerson Process Management Oy) for 10 minutes and rinsed thoroughly, followed by 10 minutes in water, ethanol, and deionized water each.

Saturation of the growth with respect of precursor pulse and purge times reported in previous studies[217,240] was verified by varying the pulse lengths one at a time in the ALD cycle. Pulse lengths are later indicated with this notation in seconds: $t_1/t_2/t_3/t_4$, where t_1 is the metal precursor pulse length, t_2 is a purge time, t_3 is the water pulse length and t_4 is the water purge time. Linear growth per cycle was evaluated by a linear fit to the film thickness as a function of the number of cycles. $BiVO_4$ films and nanolaminates were annealed in air in a Nabertherm N 7 furnace equipped with Logotherm Program Controller S19.

7.2 Film characterization

Film thicknesses were measured with X-ray reflectance (XRR) using a PANalytical X’Pert Pro MPD diffractometer and with ellipsometry using a Filmsense FS-1 multi-wavelength ellipsometer at 465, 525, 590 and 635 nm. The X-ray diffractometer was also used for grazing incidence X-ray diffraction (XRD) measurements to determine crystalline phases present in the films. High temperature XRD measurements were done in air using an Anton-Paar HTK1200N furnace stage in the diffractometer. A Hitachi S-4800 field emission scanning electron microscope (SEM) with an integrated Oxford INCA 350 energy dispersive spectrometer (EDS) was used for imaging the morphology of the films and measuring their composition. EDS results were analyzed with the GRMfilm software[260] to evaluate film composition, assuming stoichiometric oxygen content with Bi in the +3 oxidation state and V in the +5 oxidation state. Elemental depth profiles were measured with time-of-flight elastic recoil detection analysis (ToF-ERDA). Reflectance and transmittance spectra were measured with a Hitachi U-2000 spectrophotometer. An aluminum mirror was used as a reference for the reflectance measurements and the reflectance spectra were multiplied with the reference spectrum of aluminum to obtain the actual reflectivity.

8 Results and discussion

8.1 Binary oxide deposition

Bi_2O_3 was deposited from $Bi(dmb)_3$ and H_2O on Si(100) at 150 °C. The deposition process behaved as reported earlier by Hatanpää et al.,[217] except that the average GPC was slightly lower: 0.35 Å vs. 0.38 Å reported earlier for 1000 cycles. This small deviation is most likely because of some differences in the substrate surfaces, as the GPC values after the nucleation period differ only by 0.01 Å. XRD measurements also showed that the as-deposited films were tetragonal Bi_2O_3 (Figure 22a), in contrast to the amorphous Bi_2O_3 deposited at 150 °C in other studies. Modelling of the XRR results indicated film density of 8.9–9.2 g/cm^3, which is in line with the literature value of 8.9 g/cm^3 for bulk Bi_2O_3.[261] SEM image (Figure 22b) shows granular surface structure, and EDS detected no elements other than Bi and O in the samples and Si from the substrate.

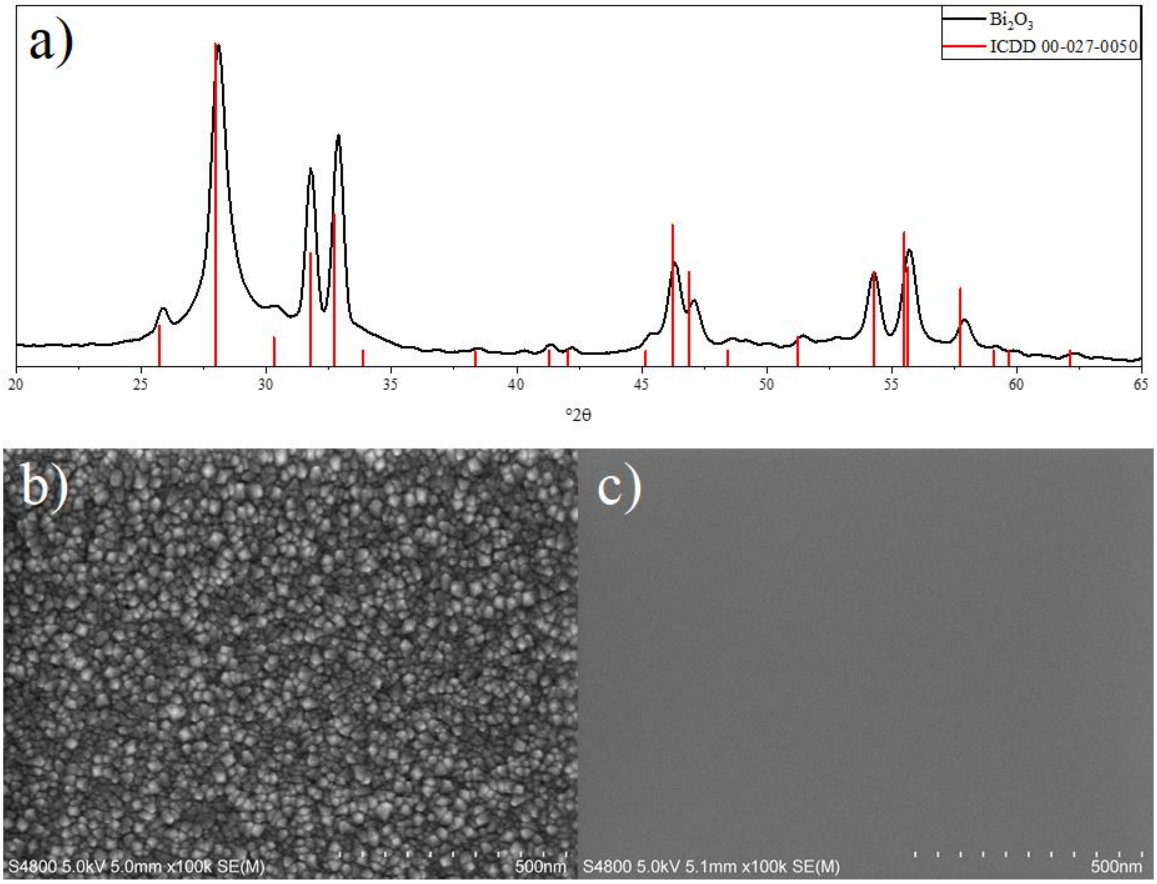

Figure 22. a) GI-XRD pattern of a Bi_2O_3 film overlaid with a reference pattern for tetragonal Bi_2O_3 and SEM images of b) a Bi_2O_3 film and c) a VO_x film deposited with ALD.

The VO_x process with TEMAV and water behaved significantly differently from that reported by Blanquart et al.[240] Firstly, it was found that an evaporation temperature of 40 °C was sufficient for TEMAV, whereas in the earlier study, using the same type of reactor, the precursor was heated to 65 °C. Other studies using TEMAV also place the evaporation temperature at 65–70 °C, but in these studies the different reactors and precursor delivery system can explain the difference.[238–240] At 65 °C the precursor was consumed very rapidly, and therefore the lowest possible evaporation temperature was used in this study.

The complete reaction of TEMAV with the surface required 3 s, double the time reported earlier. Furthermore, the average GPC values were much lower: 0.45 Å compared to about 0.60 Å reported previously.[240] The longer saturation time is probably due to a smaller precursor flux, which in turn would be caused by the low evaporation temperature. ALD precursor fluxes can also affect the saturated GPC in some cases.[262] The films were amorphous according to XRD, and SEM showed a featureless surface (Figure 22c). Only V, O, Si, and C were detected in EDS. Modelling of XRR results indicated that the densities of the films were between 4.0 and 4.4 g/cm^3. Bulk densities of VO_2 and V_2O_5 are 4.3 and 3.4 g/cm^3, respectively.[261]

8.2 $BiVO_4$ deposition

Despite the unexpected growth characteristics of VO_x, both binary oxide films were of good enough quality to continue to the $BiVO_4$ depositions. 0.5/1.0/0.5/2.0 s was chosen as the subcycle for Bi_2O_3 and 3.0/2.0/1.0/3.0 s for VO_x. To deposit $BiVO_4$, both supercycles and VO_x/Bi_2O_3 nanolaminates were investigated.

8.2.1 Supercycle approach

A simple supercycle of one Bi_2O_3 and one VO_x cycle resulted in a highly Bi-rich film according to EDS. To deposit stoichiometric films, the number of VO_x subcycles in the supercycle was increased. EDS results of films with different supercycles are presented in Table 7. A 1:2 Bi_2O_3:VO_x supercycle results in a fairly good stoichiometry already, but the supercycle can be fine-tuned further by periodically leaving out VO_x subcycles. For some reason, increasing the Bi_2O_3:VO_x cycle ratio to 7:13 actually decreased the amount of Bi. This was verified with repeated depositions. To rule out a possible source of error, the consistency of the composition along the precursor flow direction was investigated with EDS, and variation was insignificant.

Table 7. Compositions of films deposited with different supercycles as measured by EDS. Stoichiometric amount of oxygen was assumed in the calculation of the atomic concentrations. Fields marked by a dash were not measured.

Bi:V subcycle ratio	Bi concentration (at-%)	V concentration (at-%)	Bi:V atomic ratio	Bi:V atomic ratio after annealing at 450 °C
1:1	34	5	6.5	–
5:9	17	16	1.0	1.2
7:13	15	18	0.89	–
1:2	18	19	0.93	0.93
1:3	11	24	0.48	–

XRD measurements revealed that most of the bismuth gets reduced to metallic form in the supercycle approach. The (012) reflection of rhombohedral Bi at 27.2 °2θ is especially strong in the X-ray diffractograms (Figure 23), whereas other reflections are much weaker. SEM images of these films show large globules of apparently different material, presumed to be bismuth metal, on top of the films (Figure 24). As Berglund et al.[188] noted, metallic bismuth diffuses readily on surfaces, which would explain the agglomeration to globular structures.

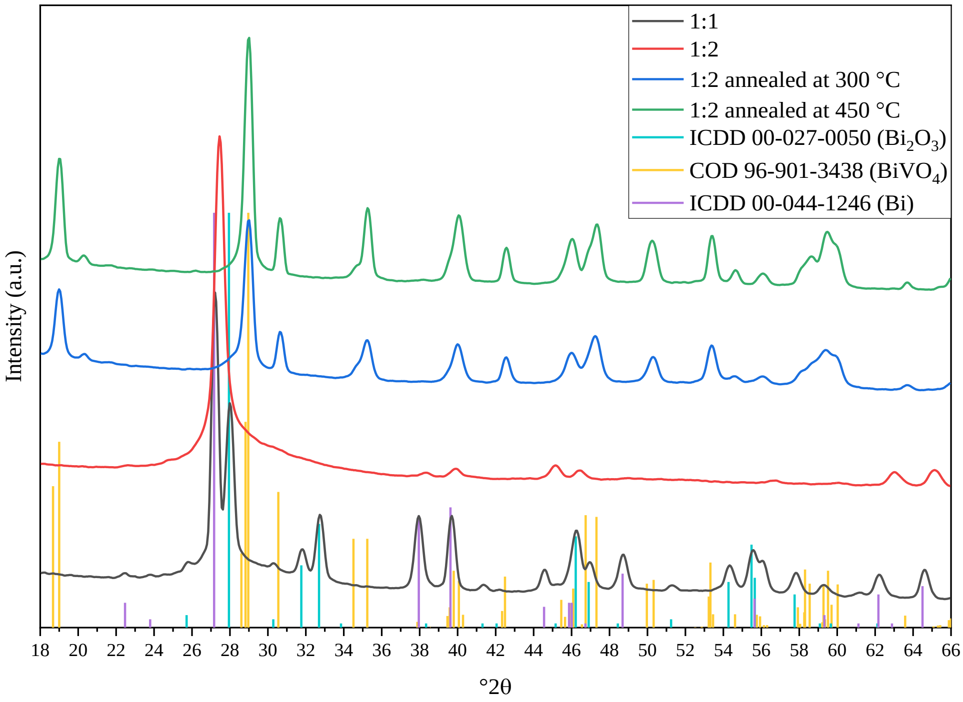

Figure 23. X-ray diffractograms of the as-deposited supercycle samples (1:1 and 1:2) and the 1:2 supercycle samples annealed at 300 and 450 °C in air. Reference diffraction patterns of tetragonal Bi_2O_3, monoclinic scheelite $BiVO_4$, and rhombohedral Bi are shown as vertical lines.

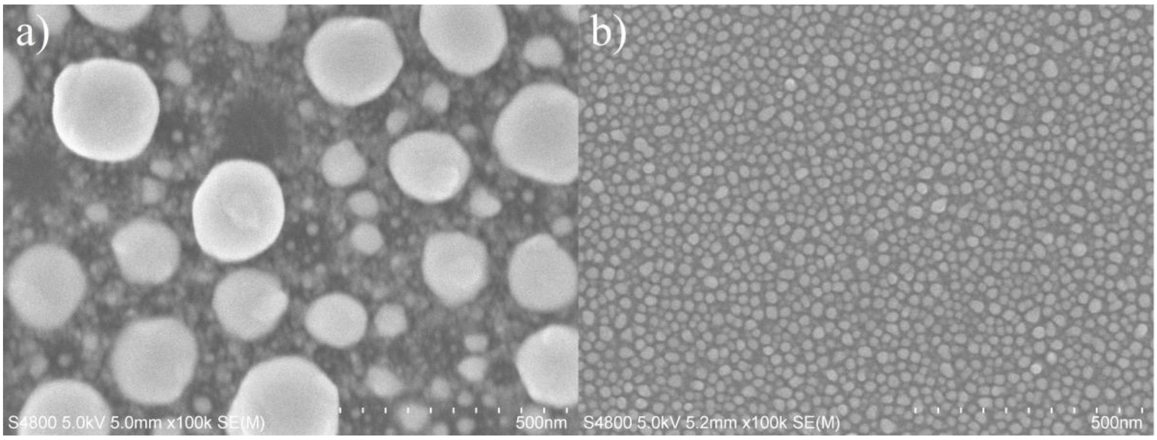

Figure 24. SEM images of unannealed $BiVO_4$ films deposited with a) 1:1 supercycles and b) 1:2 supercycles.

The reduction of bismuth in ternary ALD processes has been observed before by Schuisky et al.[259] In their study water was proposed to be the reducing agent, but that would not explain the low amount of V in the films deposited in this study. The metallic bismuth possibly inhibits VO_x nucleation somehow, but more likely TEMAV is oxidized, and vanadium leaves the surface as some volatile V(5+) species.

To test this hypothesis, the TEMAV pulse in the 1:1 supercycle process was extended to 5 s. The extended pulse resulted in an increased amount of vanadium, indicating that the TEMAV pulse takes longer to saturate after the Bi_2O_3 cycle. A supercycle without H_2O pulses was also tested and resulted in film growth. Only Bi, O and C were detected in the resulting film by EDS, and reflections of only rhombohedral Bi were observed with XRD. This experiment clearly demonstrates that TEMAV itself can reduce Bi_2O_3 to the metallic bismuth. Previous $BiVO_4$ studies do not report reduction of Bi by the pentavalent VTIP.[17–19]

The standard reduction potentials of Bi^{3+}/Bi^0 (E^0=0.317 V) and V^{5+}/V^{4+} (E^0=1.00 V) in aqueous solution do not support the idea that V^{4+} was acting as the reducing agent, but the standard reduction potentials are unlikely to reflect the situation during the ALD process. The ethylmethylamine ligand of TEMAV might act as a reducing agent, as amines have been used in the synthesis of noble metal nanoparticles.[263] Bismuth amides have been reported as ALD-precursors, but they have low thermal stability.[264] Alkyl groups of the ligands might also reduce the bismuth, for example via intermediate H_2.[265] To truly understand the mechanism by which the bismuth is reduced, further research is needed, but that is beyond the scope of this study. A stronger oxidant such as O_3 could be used to oxidize the bismuth in situ.

To re-oxidize the Bi and crystallize $BiVO_4$, the films were annealed in air. Annealing of Bi films in an oxidizing environment is a proven method to create Bi_2O_3 films.[266] 1:2 and 5:9 supercycle samples were used in the annealing studies, and the results were evaluated by XRD. A change in the color of the films from was observed visually. The samples were heated for 1 h at 300 and 450 °C in air. 300 °C was enough to see the reflections of monoclinic $BiVO_4$ in the X-ray diffractogram, but the higher temperature made some reflections a little bit clearer, likely because of improved crystallinity (Figure 23). Reflections of V_2O_5 were also weakly visible in the X-ray diffractograms of the 1:2 films, indicative of the slight excess of vanadium seen also by EDS. In some cases, the annealing increased the Bi:V atomic ratio of the samples, as in the 5:9 supercycle sample in Table 7, but neither trend nor cause for this could be identified.

To further investigate the annealing process, high temperature XRD was measured on the 1:2 supercycle sample (Figure 25). The (012) reflection of rhombohedral Bi is the only significant reflection at room temperature, but it starts diminishing at around 125 °C and disappears completely when 200 °C is reached. The crystallization of the high temperature tetragonal scheelite form of $BiVO_4$ is evident at 300 °C.

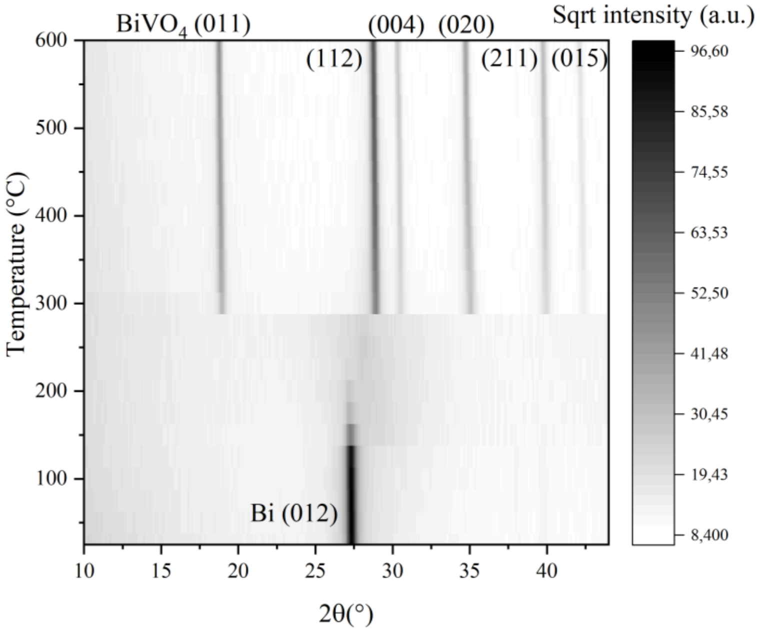

Figure 25. High temperature XRD of a 2:1 subcycle sample. The miller indices at the top of the figure refer to the tetragonal $BiVO_4$ (ICSD 99-002-1612). The diffractograms were measured at 25 °C intervals from room temperature to 600 °C. Air atmosphere was used in the experiment.

$BiVO_4$ is reported to have three main structures: tetragonal zircon, monoclinic scheelite, and tetragonal scheelite. The tetragonal scheelite has negligible photocatalytic activity.[267] The monoclinic form is thermodynamically stable at room temperature, with a reversible transformation at 255 °C to the tetragonal scheelite structure, which is metastable at room temperature.[267] XRD patterns of the two scheelite phases mainly differ by twinning of some reflections and an additional peak at 15.1° for the monoclinic structure.[267] These were hard to observe at room temperature because there was some preferred orientation of the crystallites. To verify that the films were of the monoclinic phase, another HT-XRD measurement was conducted on an already annealed $BiVO_4$ film. The gradual disappearance and reappearance of the monoclinic features was observed (Figure 26), which is consistent with the results obtained by Bierlein and Sleigh.[268] Most notable are the peaks at 15.1, 35.0 and 47.0 °2θ.

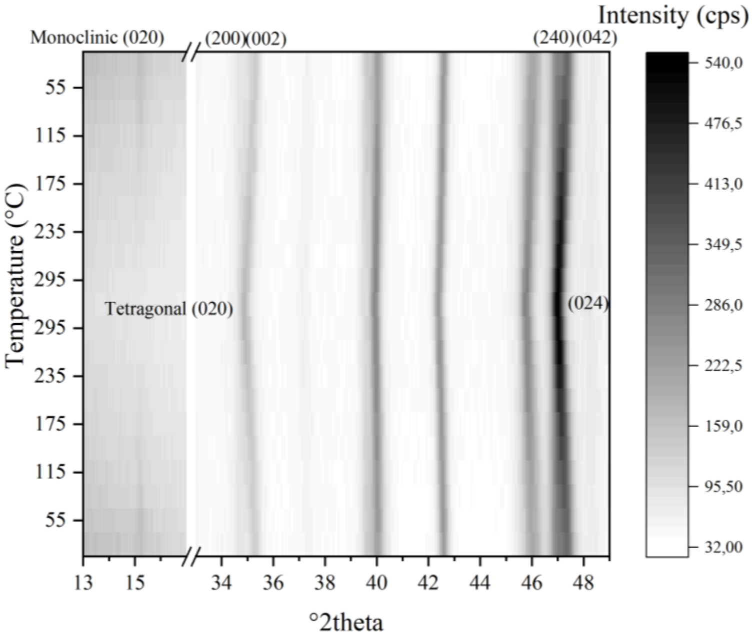

Figure 26. HT-XRD of a $BiVO_4$ film measured from room temperature (bottom of image) to 325 °C (center of image) and back to room temperature (top of image) at 30 °C intervals. Selected peaks of the monoclinic (COD 96-901-3438) and tetragonal (ICSD 99-002-1612) scheelite forms of $BiVO_4$ are indicated.

8.2.2 Nanolaminate approach

Because annealing of the films seems unavoidable in any case, nanolaminates of VO_x and Bi_2O_3 were grown to avoid the reduction of bismuth. This approach also increases the process efficiency by minimizing the amount of TEMAV lost to the side reactions. Different configurations of laminates were grown from 50 layers of 10 VO_x cycles + 10 Bi_2O_3 cycles all the way to bilayers with 1000 cycles in total. The samples along with their metal composition are listed in Table 8. XRD measurements show that even with a 4-layer structure some Bi gets reduced to the metallic form. Only a bilayer where Bi_2O_3 was grown on top of VO_x was completely free of metallic Bi, as can be seen in Figure 27.

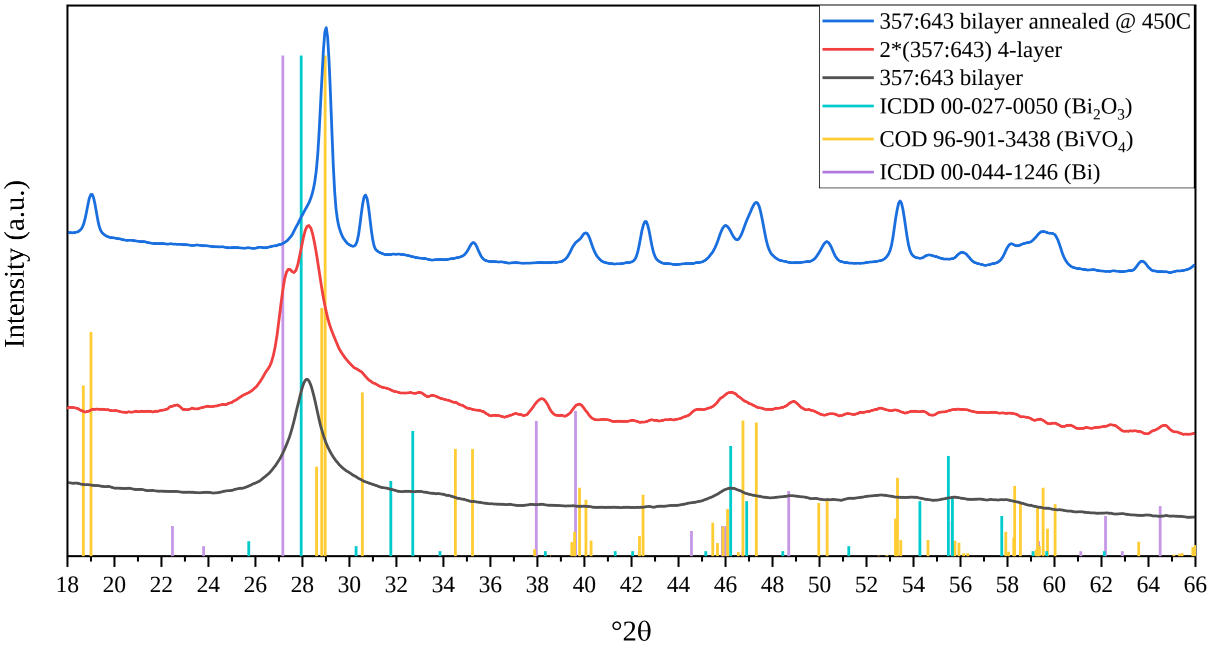

Figure 27. XRD measurements of a VO_x/Bi_2O_3 bilayer, 4-layer nanolaminate, and the bilayer sample after being annealed at 450 °C. Reference patterns for the tetragonal Bi_2O_3, monoclinic $BiVO_4$ and rhombohedral Bi are shown as vertical lines.

XRR measurements of the nanolaminates indicated that nucleation of VO_x on Bi_2O_3 takes a bit longer than vice versa, possibly because the first cycles were used up in the reduction of bismuth. This has some effect on the composition of the films grown with different layer thicknesses, but it becomes insignificant at around 100 cycles as can be seen from Table 8. The Bi to V ratio in the films (0.5) is of the order that would be expected on the basis of the growth rates and densities of the binary oxide processes (0.6). Composition along the precursor flow direction was investigated with EDS, and the variation was negligible, like in the supercycle films. After annealing the nanolaminate structures at 450 °C, monoclinic $BiVO_4$ was the dominant phase detected by XRD. In addition, reflections of V_2O_5 or Bi_2O_3 were visible in some non-stoichiometric samples.

Table 8. Compositions of VO_x/Bi_2O_3 nanolaminates with different layer thicknesses deposited with a total cycle number of 1000. The VO_x to Bi_2O_3 cycle ratio was 1:1 in all the samples except the two bilayers. Selected samples were annealed at 450 °C in air for 1 h.

Cycles	Bi concentration (at-%)	V concentration (at-%)	Bi:V atomic ratio before annealing	Bi:V atomic ratio after annealing
50x(10V+10Bi)	18	16	1.1	
10x(50V+50Bi)	14	19	0.7	
5x(100V+100Bi)	11	21	0.5	
2x(250V+250Bi)	11	21	0.5	
500V+530Bi	12	20	0.6	0.7
357V+643Bi	17	16	1.1	1.2

More detailed measurements of the composition, including impurities and elemental depth profiles (Figure 28), were done with ToF-ERDA. The full sample information and ToF-ERDA results are presented in Tables 9 and 10, respectively. The ToF-ERDA measurements were done on a series of three nanolaminate samples with different stoichiometries annealed in air at 325 °C for 1 h and two additional samples: one annealed at 450 °C for 1h and another annealed at 325 °C for 1 h but with thinner individual layers. Based on previous EDS results, a sample with 4 layers and VO_x to Bi_2O_3 cycle ratio of 370 to 630 was chosen as a baseline, and the stoichiometry series was made by varying the cycle ratio in increments of 10.

Table 9. Key properties of the $BiVO_4$ nanolaminate samples measured with ToF-ERDA.

Sample name	Cycles	annealing temperature (°C)	Bi:V atomic ratio	Impurities in total (at-%)
V-rich	2x(380V+620Bi)	325	1.05	3.7
Baseline	2x(370V+630Bi)	325	0.86	7.0
Bi-rich	2x(360V+640Bi)	325	1.00	3.6
High-T ann.	2x(370V+630Bi)	450	1.02	2.4
Thin layers	8x(90V+160Bi)	325	1.11	1.8

Table 10. Composition of $BiVO_4$ films in atomic percentage as measured with ToF-ERDA.

Sample	Bi (at-%)	V (at-%)	O (at-%)	H (at-%)	C (at-%)	N (at-%)	Cl (at-%)
V-rich	16.2±0.1	15.4±0.5	64.7±0.7	3.2±0.4	0.19±0.06	0.21±0.07	0.10±0.04
Baseline	14.5±0.1	16.8±0.5	61.8±0.6	5.6±0.6	0.59±0.13	0.61±0.13	0.18±0.07
Bi-rich	16.3±0.1	16.2±0.5	63.9±0.7	3.0±0.4	0.23±0.07	0.21±0.06	0.23±0.07
High-T	16.7±0.1	16.4±0.5	64.5±0.7	2.2±0.4	0.09±0.04	0.09±0.04	<0.01
Thin layers	17.6±0.1	15.9±0.5	64.8±0.7	1.4±0.3	0.18±0.07	0.22±0.08	<0.07

As expected, the sample annealed at 450 °C had smaller concentration of impurities than the corresponding samples annealed at 325 °C. Quite surprisingly, however, the sample with thin layers had the least impurities, mainly because of the low amount of hydrogen. This thinner-layered laminate also had a decreased amount of vanadium, probably because of the nucleation delay, which indicates that the VO_x layers are the major contributor of impurities. The nitrogen impurity in all the films also supports this notion as the decomposition of EtMeN-ligands is the most likely source of nitrogen. No source for the chlorine detected in some samples could be identified, but some possibilities are impurities in the precursors or contamination in the reactor.

The stoichiometry series did not come out exactly as intended. All the samples measured in EDS showed Bi:V ratio of 1.0–1.1, but ratios measured with ToF-ERDA were slightly lower, except in the “V-rich” sample. Accordingly, the sample aimed to be the baseline had an unexpectedly low bismuth content, while EDS measurement of the baseline sample in fact showed a ratio of 1.0. This might be caused by some error in the sample handling, as the high-T sample cleaved from the same unannealed sample had 1:1 stoichiometry, but EDS also showed similar discrepancy in the Bi content. Furthermore, the stoichiometry of the other two samples in the series was skewed opposite to what would be expected in the ToF-ERDA results. Although unlikely, one explanation for this observation would be that the two samples got mixed up. Another possibility is random fluctuation caused by sensitivity of the process to temperature and other factors. This would mean that the cycle ratio variation in the stoichiometry sample series was too small to yield much information. Aside from this, the “Bi-rich” sample had a very good stoichiometry with exactly the targeted Bi:V ratio of 1.00 as measured with ToF-ERDA.

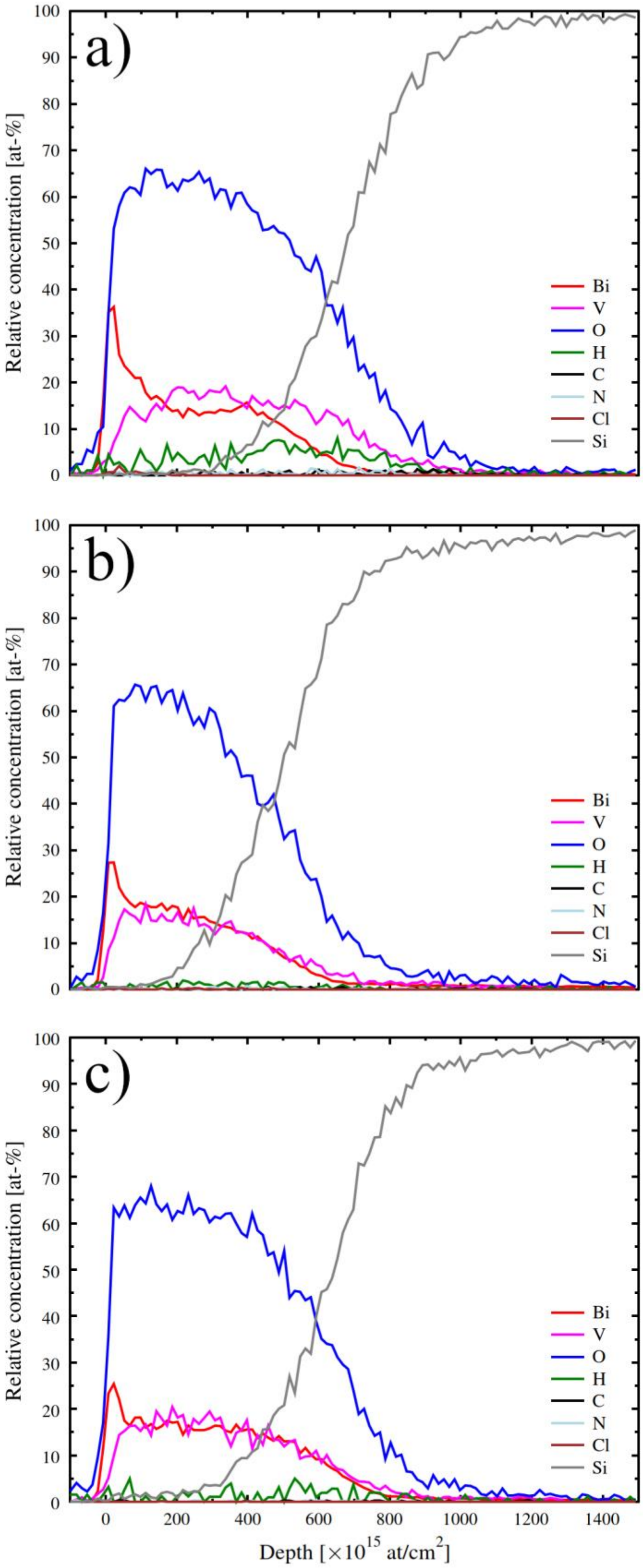

Figure 28. ToF-ERDA depth profiles of nanolaminate samples with 2x(370 VO_x and 630 Bi_2O_3 cycles) annealed in air at a) 325 °C and b) 450 °C, and c) a nanolaminate with 8x(90 VO_x and 160 Bi_2O_3 cycles) annealed at 325 °C.

An interesting finding was made with from the elemental depth profiles (Figure 28). All samples showed a significant excess of bismuth at the film surface, with a corresponding excess of vanadium toward the deeper layers. This effect was very strong in the thick laminates annealed at 325 °C but was also visible in the thin layered laminate annealed at the same temperature and the high-T sample annealed at 450 °C. For some samples the gradient was expected, as XRR showed a layered structure in the thick layered laminates still after 8 h at 325 °C (where individual layer thicknesses were around 15 nm for VO_x and 35 nm for Bi_2O_3) and some Bi_2O_3 was detected in XRD. With the thinner laminates these indicators of heterogeneity were not observed, and the samples annealed at 450 °C were too rough to measure with XRR. The excess of Bi in the top layer in combination with the large atomic mass of Bi might have screened the deeper vanadium-rich layers in EDS measurements, and EDS might also be more sensitive to the heavier metal ions. Together these factors could explain the slight difference in EDS and ToF-ERDA measurements.

In the previous nanolaminate study by Bielinski et al.,[19] the layer thicknesses were about 10 nm, and the samples were annealed at 450 °C for 2 h. The annealed films were reported to be uniform in composition as measured by cross-sectional STEM-EDS elemental mapping.[19] Presumably using a layer thickness of less than 10 nm and annealing at 450 °C would have resulted in complete mixing of the layers in the present study as well. Testing this hypothesis was attempted, but the stoichiometry of the films was unexpectedly skewed in this deposition series. Further depositions could not be carried out because of time constraints. What was learnt however, is that the process seems to be much more sensitive than expected. Two series made using the exact same method and reactor with a few months and maintenances in between resulted in very different stoichiometries. The Bi_2O_3 process by itself was tested again, because the films lacked bismuth, but nothing unexpected and extraordinary could be identified.

Morphology of the thin films was studied with SEM before (Figure 24) and after (Figure 29) annealing. Surfaces of thick-layered nanolaminates before annealing were similar to the Bi_2O_3 films (Figure 22b) whereas thinner layered laminates were closer to supercycle films (Figure 24b) in morphology. When thick (50–80 nm) films were deposited on Si(100) with the native oxide and annealed at 450 °C, the films most often formed large grains ranging in size from 10 to 300 nm, with some pinholes in between (Figure 29a). Similar morphologies were reported for ALD $BiVO_4$ films by Lamm et al.[18] and Bielinski et al.[19] and also for films made by other

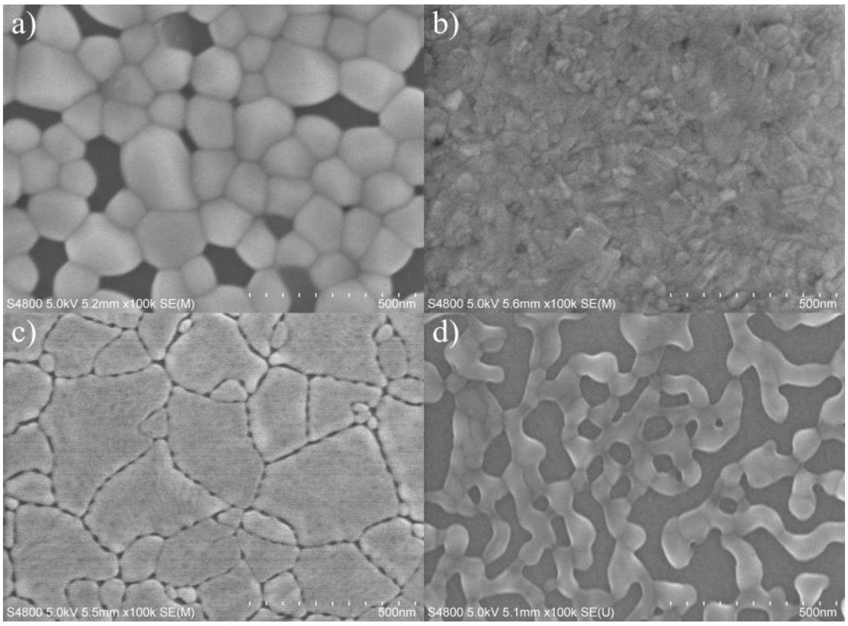

Figure 29. SEM images of annealed $BiVO_4$ films: a) 50 nm thick 2:1 supercycle film annealed at 450 °C, b) 80 nm thick nanolaminate annealed at 450 °C (VO_x to Bi_2O_3 cycle ratio 357:643) and a 10 nm bilayer (92 cycles VO_x and 144 cycles Bi_2O_3) annealed at c) 325 °C and d) 450 °C.

methods, such as drop casting[183] and spray pyrolysis.[16] In some cases our films were nearly continuous, like in Figure 29b, but they suffered from blistering and partial delamination.

Very thin films had particularly poor coverage when annealed at high temperatures and mostly consisted of separate particles or strands. Even the sample annealed at 325 °C does not completely cover the substrate (Figure 29c). Similar results were obtained when 10 nm thick films deposited using the supercycle approach were annealed. It seems that $BiVO_4$ reforms (recrystallizes) easily at high temperatures and completely pinhole-free films are difficult to achieve, which is unfortunate, because exposed conductor surfaces might facilitate back-reactions in photoelectrochemical systems. $BiVO_4$ might behave differently on other substrates, however, and even if pinholes cannot be completely avoided, they can be fixed with selectively deposited passivation layers.[204]

8.2.3 Optical characterization

For optical studies, three films with somewhat different stoichiometries were grown on Al_2O_3-passivated soda-lime glass. They were deposited as 4-layer nanolaminates and annealed in air for 1 h at 450 °C. Final film thickness (d) was approximately 85 nm. Reflectance (R) and transmittance (T) of the films were measured (Figure 30). From these the absorption coefficient (α) was calculated according to the equation:

$$\alpha = -\frac{\ln{(T+R)}}{d}, \tag{2}$$

The absorption coefficient is related to a photon energy $h\nu$ and band gap E_g by the Tauc relation:

$$(\alpha h\nu)^n = B(E_g - h\nu), \tag{3}$$

where B is a material specific constant and n is a constant that depends on the nature of the band gap. For a direct allowed band gap $n = 2$ and for an indirect allowed band gap $n = \frac{1}{2}$. For a true semiconductor material plotting $(\alpha h\nu)^n$ against photon energy results in a plot with a distinct linear area. Extrapolating this linear part to the $h\nu$-axis gives an estimate of the band gap of the material. With materials that have considerable doping or other intraband gap states, however, the absorption spectrum shows an Urbach tail, which distorts the Tauc plot. In this case linear extrapolation to the $h\nu$-axis results in large errors in the estimated band gap. Makuła et al.[269]

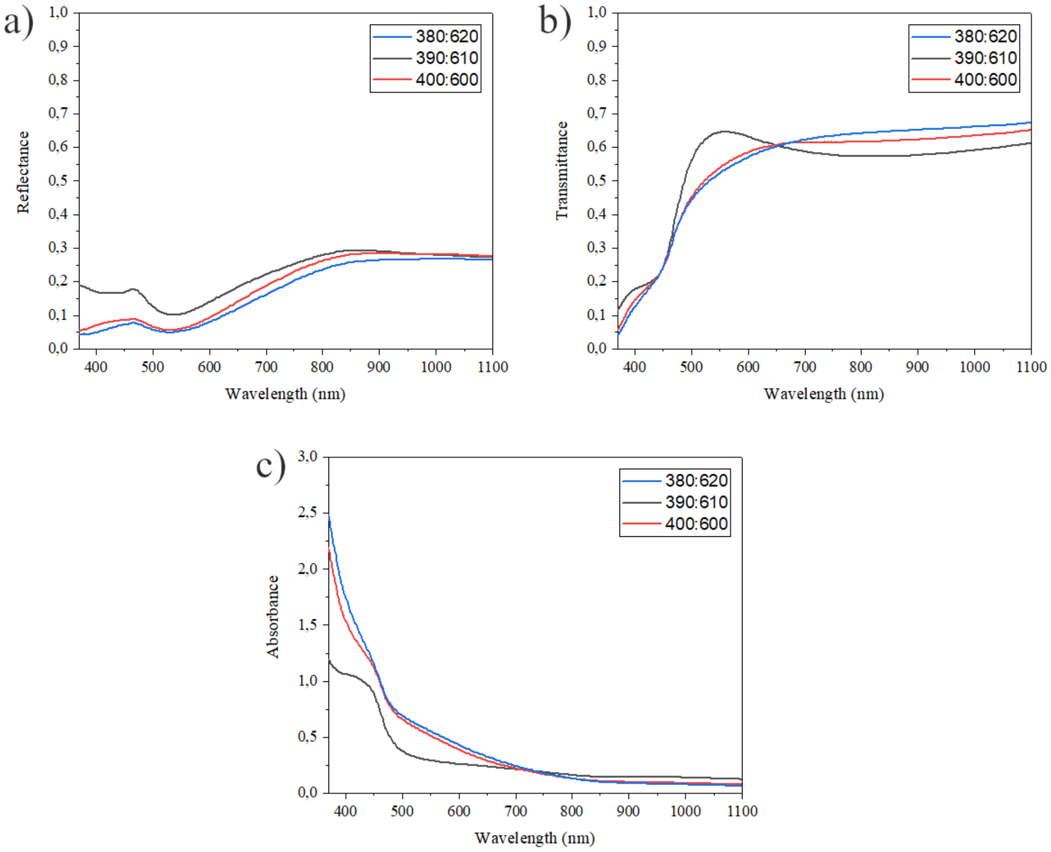

Figure 30. a) Reflectance (R), b) transmittance (T), and c) absorbtion coefficient (α) spectra of three BiVO4 films of varying stoichiometries made by annealing VO_x/Bi_2O_3 nanolaminates.

proposed a method where another linear extrapolation from the Urbach tail is used as a baseline. The estimated band gap energy is the value of *hv* at the intersection of the two lines. Tauc plots of the spectra recorded here are presented in Figure 31.

The spectra show evidence of Urbach tails, possibly caused by impurity states or incomplete crystallization. By using the method described by Makuła et al., the band gaps of all the films were approximated to be close to 2.5 eV. This value is in good agreement with the literature,[7] but the Urbach tails are much larger than expected; similar absorption at long wavelengths was reported only by Stefik[17]. They did not employ correction methods and instead reported band gaps of 2.24 and 2.28 eV approximated by simple extrapolation of the Tauc plots. Band gaps of the films in the present study range from 1.95 to 2.22 eV when analyzed this way. Band gap energies for the whole series calculated in these two ways are presented in Table 11.

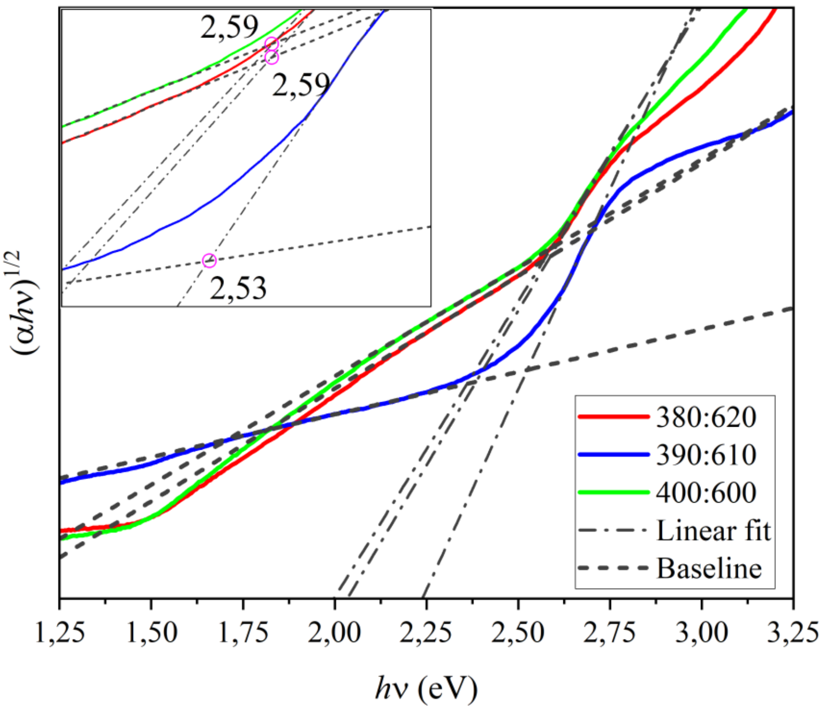

Figure 31. Tauc plots of $BiVO_4$ films made by annealing VO_x/Bi_2O_3 nanolaminates. VO_x:Bi_2O_3 cycle ratios are in the legend. Inset shows the intercections of the linear fits and baselines as well as the hv value at that point.

Table 11. Band gap energies of films with different stoichiometries.

VO_x/Bi_2O_3 cycle ratio	Bi:V atomic ratio by EDS	E_g without baseline (eV)	E_g with baseline (eV)
380:620	1.1	2.03	2.59
390:610	1.0	2.24	2.53
400:600	0.9	2.00	2.59

It is to be noted that the films that were studied in UV-vis spectrometry were deposited before the ToF-ERDA analysis. For this reason, the laminate layers were so thick that the annealing apparently was not able to completely mix the layers. Further, the Bi:V atomic ratio measured with EDS might be slightly higher than the true values as discussed with the ToF-ERDA measurements. These factors probably affected the optical properties, and the variation the composition of the films very likely caused the strong Urbach tails.

9 Conclusions

In this study a new $BiVO_4$ ALD process using $Bi(dmb)_3$, TEMAV, and water as precursors was developed and studied. Both supercycle- and nanolaminate-based methods were employed. Both methods require annealing in air after the deposition to achieve the $BiVO_4$ films. Some Bi_2O_3 is reduced to the metallic bismuth regardless of the method if it encounters TEMAV, which is a major drawback of this precursor combination. In the supercycle method the reduction is even more significant as most of the Bi_2O_3 is reduced, which also means that a lot of TEMAV is lost in the side reaction. Thus, the nanolaminate approach is more efficient in terms of precursor usage. The crystallization to monoclinic $BiVO_4$ upon annealing was observed at temperatures as low as 300 °C by HT-XRD, but a higher annealing temperature of 450 °C increased crystallinity. For proper mixing of the nanolaminates at least 450 °C is required, and even then, the individual layer thicknesses should be kept below 10 nm to ensure a uniform composition in a reasonable time.

With the supercycle samples the best stoichiometry was achieved with the Bi_2O_3 to VO_x subcycle ratio of 5:9. For the nanolaminates with sufficiently thin layers no conclusive results could be obtained, but a good starting point for further studies would be a repetition of 100 cycles of VO_x and 150 cycles of Bi_2O_3. However, it should be kept in mind that process conditions had a large effect on the stoichiometry. ToF-ERDA studies of the nanolaminates showed that only low amounts of impurities are left in the films, especially after the annealing at 450 °C. Most of the impurities seem to originate from the VO_x films, as carbon was detectable in the binary VO_x film even with EDS.

On native SiO_2 and ALD-grown Al_2O_3 the $BiVO_4$ films are difficult to make continuous, and in some cases they suffer from delamination. The problems with morphology and adhesion can possibly be avoided by using other substrates or interfacial layers. Optical properties of the films deposited as nanolaminates were investigated and, despite the possibly incomplete mixing of the laminate layers, the band gaps were close to the values reported previously. However, the spectra did show evidence of a large amount of intraband gap states. To see if these are due to incomplete mixing of the films, better optimized nanolaminates should be studied.

Future research should focus on investigating why the nanolaminate process is so sensitive to the process conditions. If that issue can be solved, the composition of the resulting films can be further optimized. Other research topics arising from the observations in this study are the morphology of $BiVO_4$ grown on different substrates and the interaction between $Bi(dmb)_3$ and TEMAV. The latter could be studied by analyzing residual gases from their reactions.

As discussed in the literature part of the thesis, ALD $BiVO_4$ has already been applied to photocatalysis and for fabrication of nanostructured photoanodes. There is no reason to believe that the films deposited here are unsuitable for photocatalysis, and their performance in comparison to the earlier reports should be studied. To further make use of the possibilities afforded by ALD, doping the films with metals such as W and Mo could be attempted. Advanced configurations like gradient doping and incorporation of interlayers are simple to implement because of the characteristics of ALD.

10 References

1 A. J. Esswein and D. G. Nocera, *Chem Rev*, 2007, **107**, 4022–4047.

2 T. Hisatomi, J. Kubota and K. Domen, *Chem Soc Rev*, 2014, **43**, 7520–7535.

3 M. Pelaez, N. T. Nolan, S. C. Pillai, M. K. Seery, P. Falaras, A. G. Kontos, P. S. M. Dunlop, J. W. J. Hamilton, J. A. Byrne, K. O'Shea, M. H. Entezari and D. D. Dionysiou, *Appl Catal B*, 2012, **125**, 331–349.

4 I. P. Parkin and R. G. Palgrave, *J Mater Chem*, 2005, **15**, 1689–1695.

5 Y. Zhang, N. Zhang, Z.-R. Tang and Y.-J. Xu, *Chem Sci*, 2013, **4**, 1820–1824.

6 I. Dincer and C. Acar, *Int J Hydrogen Energy*, 2015, **40**, 11094–11111.

7 J. K. Cooper, S. Gul, F. M. Toma, L. Chen, Y.-S. Liu, J. Guo, J. W. Ager, J. Yano and I. D. Sharp, *The Journal of Physical Chemistry C*, 2015, **119**, 2969–2974.

8 M. A. Holmes, T. K. Townsend and F. E. Osterloh, *Chemical Communications*, 2012, **48**, 371–373.

9 M. Trochowski, M. Kobielusz, K. Mróz, M. Surówka, J. Hämäläinen, T. Iivonen, M. Leskelä and W. Macyk, *J Mater Chem A Mater*, 2019, **7**, 25142–25154.

10 T. Suntola, *Thin Solid Films*, 1992, **216**, 84–89.

11 R. W. Johnson, A. Hultqvist and S. F. Bent, *Materials Today*, 2014, **17**, 236–246.

12 A. J. M. Mackus, J. R. Schneider, C. MacIsaac, J. G. Baker and S. F. Bent, *Chemistry of Materials*, 2019, **31**, 1142–1183.

13 V. Miikkulainen, M. Leskelä, M. Ritala and R. L. Puurunen, *J Appl Phys*, 2013, **113**, 21301.

14 H. Kim, *Thin Solid Films*, 2011, **519**, 6639–6644.

15 N. Pastukhova, A. Mavrič and Y. Li, *Adv Mater Interfaces*, 2021, **8**, 2002100.

16 F. F. Abdi, T. J. Savenije, M. M. May, B. Dam and R. van de Krol, *J Phys Chem Lett*, 2013, **4**, 2752–2757.

17 M. Stefik, *ChemSusChem*, 2016, **9**, 1727–1735.

18 B. Lamm, A. Sarkar and M. Stefik, *J Mater Chem A Mater*, 2017, **5**, 6060–6069.

19 A. R. Bielinski, S. Lee, J. J. Brancho, S. L. Esarey, A. J. Gayle, E. Kazyak, K. Sun, B. M. Bartlett and N. P. Dasgupta, *Chemistry of Materials*, 2019, **31**, 3221–3227.

20 W. H. Strehlow and E. L. Cook, *J Phys Chem Ref Data*, 1973, **2**, 163–200.

21 R. Enderlein and N. J. Horing, *Fundamentals Of Semiconductor Physics And Devices*, World Scientific, Singapore, 1997.

22 A. M. Appel and M. L. Helm, *ACS Catal*, 2014, **4**, 630–633.

23 A. J. Nozik and R. Memming, *J Phys Chem*, 1996, **100**, 13061–13078.

24 K. Maeda and K. Domen, *The Journal of Physical Chemistry C*, 2007, **111**, 7851–7861.

25 S. E. Braslavsky, A. M. Braun, A. E. Cassano, A. v Emeline, M. I. Litter, L. Palmisano, V. N. Parmon and N. Serpone, *Pure and Applied Chemistry*, 2011, **83**, 931–1014.

26 Z. Chen, T. F. Jaramillo, T. G. Deutsch, A. Kleiman-Shwarsctein, A. J. Forman, N. Gaillard, R. Garland, K. Takanabe, C. Heske, M. Sunkara, E. W. McFarland, K. Domen, E. L. Miller, J. A. Turner and H. N. Dinh, *J Mater Res*, 2010, **25**, 3–16.

27 F. F. Abdi, N. Firet and R. van de Krol, *ChemCatChem*, 2013, **5**, 490–496.

28 M. R. Hoffmann, S. T. Martin, W. Choi and D. W. Bahnemann, *Chem Rev*, 1995, **95**, 69–96.

29 K. P. S. Parmar, H. J. Kang, A. Bist, P. Dua, J. S. Jang and J. S. Lee, *ChemSusChem*, 2012, **5**, 1926–1934.

30 E. M. P. Steinmiller and K.-S. Choi, *Proceedings of the National Academy of Sciences*, 2009, **106**, 20633–20636.

31 R. Li, F. Zhang, D. Wang, J. Yang, M. Li, J. Zhu, X. Zhou, H. Han and C. Li, *Nat Commun*, 2013, **4**, 1432.

32 J. Schneider and D. W. Bahnemann, *J Phys Chem Lett*, 2013, **4**, 3479–3483.

33 K. Maeda, K. Teramura, D. Lu, N. Saito, Y. Inoue and K. Domen, *Angewandte Chemie International Edition*, 2006, **45**, 7806–7809.

34 M. Liao, J. Feng, W. Luo, Z. Wang, J. Zhang, Z. Li, T. Yu and Z. Zou, *Adv Funct Mater*, 2012, **22**, 3066–3074.

35 A. A. Adesina, *Catalysis Surveys from Asia*, 2004, **8**, 265–273.

36 A. Fujishima and X. Zhang, *Comptes Rendus Chimie*, 2006, **9**, 750–760.

37 Z. Wang, P. K. Nayak, J. A. Caraveo-Frescas and H. N. Alshareef, *Advanced Materials*, 2016, **28**, 3831–3892.

38 T. Yao, X. An, H. Han, J. Q. Chen and C. Li, *Adv Energy Mater*, 2018, **8**, 1800210.

39 T. Bak, M. K. Nowotny, L. R. Sheppard and J. Nowotny, *The Journal of Physical Chemistry C*, 2008, **112**, 12981–12987.

40 Y. J. Hwang, C. Hahn, B. Liu and P. Yang, *ACS Nano*, 2012, **6**, 5060–5069.

41 M. Tordjman, K. Weinfeld and R. Kalish, *Appl Phys Lett*, 2017, **111**, 111601.

42 A. Soudi, P. Dhakal and Y. Gu, *Appl Phys Lett*, 2010, **96**, 253115.

43 A. Janotti and C. G. van de Walle, *Reports on Progress in Physics*, 2009, **72**, 126501.

44 M. Fleischer, H. Meixner and C. Tragut, *Journal of the American Ceramic Society*, 1992, **75**, 1666–1668.

45 K. van Benthem, C. Elsässer and R. H. French, *J Appl Phys*, 2001, **90**, 6156–6164.

46 O. N. Tufte and P. W. Chapman, *Physical Review*, 1967, **155**, 796–802.

47 H. P. Maruska and A. K. Ghosh, *Solar Energy Materials*, 1979, **1**, 237–247.

48 K. Yin, M. Li, Y. Liu, C. He, F. Zhuge, B. Chen, W. Lu, X. Pan and R.-W. Li, *Appl Phys Lett*, 2010, **97**, 042101.

49 M. M. El-Desoky, M. M. Mostafa, M. S. Ayoub and M. A. Ahmed, *Journal of Materials Science: Materials in Electronics*, 2015, **26**, 6793–6800.

50 C. Y. Cummings, F. Marken, L. M. Peter, K. G. Upul Wijayantha and A. A. Tahir, *J Am Chem Soc*, 2012, **134**, 1228–1234.

51 X. Zhang, H. Li, S. Wang, F.-R. F. Fan and A. J. Bard, *The Journal of Physical Chemistry C*, 2014, **118**, 16842–16850.

52 B. S. Li, K. Akimoto and A. Shen, *J Cryst Growth*, 2009, **311**, 1102–1105.

53 A. Walsh, Y. Yan, M. N. Huda, M. Al-Jassim and S.-H. Wei, *Chemistry of Materials*, 2009, **21**, 547–551.

54 H. S. Park, H.-W. Ha, R. S. Ruoff and A. J. Bard, *Journal of Electroanalytical Chemistry*, 2014, **716**, 8–15.

55 M. D. Hernández-Alonso, F. Fresno, S. Suárez and J. M. Coronado, *Energy Environ Sci*, 2009, **2**, 1231–1257.

56 S. Shen, S. A. Lindley, X. Chen and J. Z. Zhang, *Energy Environ Sci*, 2016, **9**, 2744–2775.

57 ISO, 2007. *ISO 21348:2007 Definitions of Solar Irradiance Spectral Categories.*

58 Y. Park, K. J. McDonald and K.-S. Choi, *Chem Soc Rev*, 2013, **42**, 2321–2337.

59 C. Zachäus, F. F. Abdi, L. M. Peter and R. van de Krol, *Chem Sci*, 2017, **8**, 3712–3719.

60 D. K. Zhong, S. Choi and D. R. Gamelin, *J Am Chem Soc*, 2011, **133**, 18370–18377.

61 H. S. Park, K. E. Kweon, H. Ye, E. Paek, G. S. Hwang and A. J. Bard, *The Journal of Physical Chemistry C*, 2011, **115**, 17870–17879.

62 Y. Bessekhouad, D. Robert and J.-V. Weber, *Catal Today*, 2005, **101**, 315–321.

63 L. Wu, L. Tsui, N. Swami and G. Zangari, *The Journal of Physical Chemistry C*, 2010, **114**, 11551–11556.

64 I. Sullivan, B. Zoellner and P. A. Maggard, *Chemistry of Materials*, 2016, **28**, 5999–6016.

65 C.-Y. Lin, Y.-H. Lai, D. Mersch and E. Reisner, *Chem Sci*, 2012, **3**, 3482–3487.

66 C. G. Read, Y. Park and K.-S. Choi, *J Phys Chem Lett*, 2012, **3**, 1872–1876.

67 P. P. Sahoo, B. Zoellner and P. A. Maggard, *J Mater Chem A Mater*, 2015, **3**, 4501–4509.

68 N. Koriche, A. Bouguelia, A. Aider and M. Trari, *Int J Hydrogen Energy*, 2005, **30**, 693–699.

69 R. F. G. Gardner, F. Sweett and D. W. Tanner, *Journal of Physics and Chemistry of Solids*, 1963, **24**, 1175–1181.

70 C. Sanchez, K. D. Sieber and G. A. Somorjai, *J Electroanal Chem Interfacial Electrochem*, 1988, **252**, 269–290.

71 A. Kay, I. Cesar and M. Grätzel, *J Am Chem Soc*, 2006, **128**, 15714–15721.

72 O. Zandi, B. M. Klahr and T. W. Hamann, *Energy Environ Sci*, 2013, **6**, 634–642.

73 J. Wang, J. B. Neaton, H. Zheng, V. Nagarajan, S. B. Ogale, B. Liu, D. Viehland, V. Vaithyanathan, D. G. Schlom, U. v Waghmare, N. A. Spaldin, K. M. Rabe, M. Wuttig and R. Ramesh, *Science (1979)*, 2003, **299**, 1719–1722.

74 S.-M. Lam, J.-C. Sin and A. R. Mohamed, *Mater Res Bull*, 2017, **90**, 15–30.

75 F. Gao, Y. Yuan, K. F. Wang, X. Y. Chen, F. Chen, J.-M. Liu and Z. F. Ren, *Appl Phys Lett*, 2006, **89**, 102506.

76 F. Gao, X. Y. Chen, K. B. Yin, S. Dong, Z. F. Ren, F. Yuan, T. Yu, Z. G. Zou and J.-M. Liu, *Advanced Materials*, 2007, **19**, 2889–2892.

77 S. Bharathkumar, M. Sakar and S. Balakumar, *The Journal of Physical Chemistry C*, 2016, **120**, 18811–18821.

78 J. Luo and P. A. Maggard, *Advanced Materials*, 2006, **18**, 514–517.

79 A. K. L. Sajjad, S. Shamaila, B. Tian, F. Chen and J. Zhang, *Appl Catal B*, 2009, **91**, 397–405.

80 W. Yu, J. Chen, T. Shang, L. Chen, L. Gu and T. Peng, *Appl Catal B*, 2017, **219**, 693–704.

81 G. Colón, M. C. Hidalgo, J. A. Navío, E. Pulido Melián, O. González Díaz and J. M. Doña Rodríguez, *Appl Catal B*, 2008, **83**, 30–38.

82 T. Cao, Y. Li, C. Wang, C. Shao and Y. Liu, *Langmuir*, 2011, **27**, 2946–2952.

83 K. M. Lee, C. W. Lai, K. S. Ngai and J. C. Juan, *Water Res*, 2016, **88**, 428–448.

84 A. Sclafani, L. Palmisano, G. Marcí and A. M. Venezia, *Solar Energy Materials and Solar Cells*, 1998, **51**, 203–219.

85 J. Fujisawa, T. Eda and M. Hanaya, *Chem Phys Lett*, 2017, **685**, 23–26.

86 Y. Kikuchi, K. Sunada, T. Iyoda, K. Hashimoto and A. Fujishima, *J Photochem Photobiol A Chem*, 1997, **106**, 51–56.

87 M. Anne. Fox and M. T. Dulay, *Chem Rev*, 1993, **93**, 341–357.

88 K. T. Ranjit and B. Viswanathan, *J Photochem Photobiol A Chem*, 1997, **108**, 79–84.

89 X. Chen, S. Shen, L. Guo and S. S. Mao, *Chem Rev*, 2010, **110**, 6503–6570.

90 D. Kato, K. Hongo, R. Maezono, M. Higashi, H. Kunioku, M. Yabuuchi, H. Suzuki, H. Okajima, C. Zhong, K. Nakano, R. Abe and H. Kageyama, *J Am Chem Soc*, 2017, **139**, 18725–18731.

91 S. Balaz, S. H. Porter, P. M. Woodward and L. J. Brillson, *Chemistry of Materials*, 2013, **25**, 3337–3343.

92 C. M. Fang, G. A. de Wijs, E. Orhan, G. de With, R. A. de Groot, H. T. Hintzen and R. Marchand, *Journal of Physics and Chemistry of Solids*, 2003, **64**, 281–286.

93 A. Ziani, E. Nurlaela, D. S. Dhawale, D. A. Silva, E. Alarousu, O. F. Mohammed and K. Takanabe, *Physical Chemistry Chemical Physics*, 2015, **17**, 2670–2677.

94 M. de Respinis, M. Fravventura, F. F. Abdi, H. Schreuders, T. J. Savenije, W. A. Smith, B. Dam and R. van de Krol, *Chemistry of Materials*, 2015, **27**, 7091–7099.

95 E. Nurlaela, A. Ziani and K. Takanabe, *Mater Renew Sustain Energy*, 2016, **5**, 18.

96 I. Narkeviciute, P. Chakthranont, A. J. M. Mackus, C. Hahn, B. A. Pinaud, S. F. Bent and T. F. Jaramillo, *Nano Lett*, 2016, **16**, 7565–7572.

97 A. Suzuki, Y. Hirose, D. Oka, S. Nakao, T. Fukumura, S. Ishii, K. Sasa, H. Matsuzaki and T. Hasegawa, *Chemistry of Materials*, 2014, **26**, 976–981.

98 S. Melinte, A. Jeflea, M. Moise and N. Mateescu, *Journal of the Less Common Metals*, 1983, **95**, 99–103.

99 R. K. Pandey, R. B. Gore and A. J. N. Rooz, *J Phys D Appl Phys*, 1987, **20**, 1059–1062.

100 L. Tarricone, N. Romeo, G. Sberveglieri and S. Mora, *Solar Energy Materials*, 1982, **7**, 343–350.

101 R. Scheer and H. J. Lewerenz, *J Appl Phys*, 1995, **77**, 2006–2009.

102 D. C. Look and J. C. Manthuruthil, *Journal of Physics and Chemistry of Solids*, 1976, **37**, 173–180.

103 M. ben Rabeh, N. Khedmi, M. A. Fodha and M. Kanzari, *Energy Procedia*, 2014, **44**, 52–60.

104 J. F. Reber and K. Meier, *J Phys Chem*, 1984, **88**, 5903–5913.

105 A. Dey, S. Middya, R. Jana, M. Das, J. Datta, A. Layek and P. P. Ray, *Journal of Materials Science: Materials in Electronics*, 2016, **27**, 6325–6335.

106 W.-J. Chun, A. Ishikawa, H. Fujisawa, T. Takata, J. N. Kondo, M. Hara, M. Kawai, Y. Matsumoto and K. Domen, *J Phys Chem B*, 2003, **107**, 1798–1803.

107 C. M. Fang, E. Orhan, G. A. de Wijs, H. T. Hintzen, R. A. de Groot, R. Marchand, J.-Y. Saillard and G. de With, *J Mater Chem*, 2001, **11**, 1248–1252.

108 G. Hitoki, T. Takata, J. N. Kondo, M. Hara, H. Kobayashi and K. Domen, *Chemical Communications*, 2002, 1698–1699.

109 M. Hara, G. Hitoki, T. Takata, J. N. Kondo, H. Kobayashi and K. Domen, *Catal Today*, 2003, **78**, 555–560.

110 D. Yamasita, T. Takata, M. Hara, J. N. Kondo and K. Domen, *Solid State Ion*, 2004, **172**, 591–595.

111 K. Maeda, D. Lu and K. Domen, *Angewandte Chemie International Edition*, 2013, **52**, 6488–6491.

112 K. Maeda, K. Teramura, T. Takata, M. Hara, N. Saito, K. Toda, Y. Inoue, H. Kobayashi and K. Domen, *J Phys Chem B*, 2005, **109**, 20504–20510.

113 K. Teramura, K. Maeda, T. Saito, T. Takata, N. Saito, Y. Inoue and K. Domen, *J Phys Chem B*, 2006, **110**, 4500–4501.

114 T. Ohno, L. Bai, T. Hisatomi, K. Maeda and K. Domen, *J Am Chem Soc*, 2012, **134**, 8254–8259.

115 A. B. Ellis, S. W. Kaiser and M. S. Wrighton, *J Am Chem Soc*, 1976, **98**, 6855–6866.

116 A. B. Ellis, S. W. Kaiser and M. S. Wrighton, *J Am Chem Soc*, 1976, **98**, 6418–6420.

117 L. Zheng, Y. Xu, Y. Song, C. Wu, M. Zhang and Y. Xie, *Inorg Chem*, 2009, **48**, 4003–4009.

118 B. Koo, S.-W. Nam, R. Haight, S. Kim, S. Oh, M. Cho, J. Oh, J. Y. Lee, B. T. Ahn and B. Shin, *ACS Appl Mater Interfaces*, 2017, **9**, 5279–5287.

119 J. Cai, Y. Xia, R. Gang, S. He and S. Komarneni, *Appl Catal B*, 2022, **314**, 121486.

120 Y. Bessekhouad, M. Mohammedi and M. Trari, *Solar Energy Materials and Solar Cells*, 2002, **73**, 339–350.

121 X. Gao, H. bin Wu, L. Zheng, Y. Zhong, Y. Hu and X. W. (David) Lou, *Angewandte Chemie International Edition*, 2014, **53**, 5917–5921.

122 J. Cao, B. Xu, H. Lin, B. Luo and S. Chen, *Dalton Transactions*, 2012, **41**, 11482–11490.

123 X. Zong, H. Yan, G. Wu, G. Ma, F. Wen, L. Wang and C. Li, *J Am Chem Soc*, 2008, **130**, 7176–7177.

124 J. Zhang, F. Shi, J. Lin, D. Chen, J. Gao, Z. Huang, X. Ding and C. Tang, *Chemistry of Materials*, 2008, **20**, 2937–2941.

125 K.-L. Zhang, C.-M. Liu, F.-Q. Huang, C. Zheng and W.-D. Wang, *Appl Catal B*, 2006, **68**, 125–129.

126 J. Jiang, K. Zhao, X. Xiao and L. Zhang, *J Am Chem Soc*, 2012, **134**, 4473–4476.

127 L. Ye, L. Tian, T. Peng and L. Zan, *J Mater Chem*, 2011, **21**, 12479–12484.

128 H. Suzuki, M. Higashi, H. Kunioku, R. Abe and A. Saeki, *ACS Energy Lett*, 2019, **4**, 1572–1578.

129 R. C. Newman, *Reports on Progress in Physics*, 1982, **45**, 1163–1210.

130 P. A. Iles, *Solar Cells*, 1982, **7**, 79–86.

131 C. Gutsche, R. Niepelt, M. Gnauck, A. Lysov, W. Prost, C. Ronning and F.-J. Tegude, *Nano Lett*, 2012, **12**, 1453–1458.

132 C. R. Cox, M. T. Winkler, J. J. H. Pijpers, T. Buonassisi and D. G. Nocera, *Energy Environ Sci*, 2013, **6**, 532–538.

133 P. A. Kohl and F. W. Ostermayer, *Annual Review of Materials Science*, 1989, **19**, 379–399.

134 M. L. Young and D. R. Wight, *J Phys D Appl Phys*, 1974, **7**, 1824–1837.

135 V. Diadiuk, S. H. Groves, C. A. Armiento and C. E. Hurwitz, *Appl Phys Lett*, 1983, **42**, 892–894.

136 N. M. Haegel, T. Christian, C. Scandrett, A. G. Norman, A. Mascarenhas, P. Misra, T. Liu, A. Sukiasyan, E. Pickett and H. Yuen, *Appl Phys Lett*, 2014, **105**, 202116.

137 F. J. Schultes, T. Christian, R. Jones-Albertus, E. Pickett, K. Alberi, B. Fluegel, T. Liu, P. Misra, A. Sukiasyan, H. Yuen and N. M. Haegel, *Appl Phys Lett*, 2013, **103**, 242106.

138 J. Yang, K. Walczak, E. Anzenberg, F. M. Toma, G. Yuan, J. Beeman, A. Schwartzberg, Y. Lin, M. Hettick, A. Javey, J. W. Ager, J. Yano, H. Frei and I. D. Sharp, *J Am Chem Soc*, 2014, **136**, 6191–6194.

139 H. Shu, S. M. R., B. J. A., L. Michael, B. B. S. and L. N. S., *Science (1979)*, 2014, **344**, 1005–1009.

140 K. Sun, Y. Kuang, E. Verlage, B. S. Brunschwig, C. W. Tu and N. S. Lewis, *Adv Energy Mater*, 2015, **5**, 1402276.

141 J. Gu, Y. Yan, J. L. Young, K. X. Steirer, N. R. Neale and J. A. Turner, *Nat Mater*, 2016, **15**, 456–460.

142 J. Novák, S. Hasenöhrl, R. Kúdela, M. Kucera, M. I. Alonso and M. Garriga, *Materials Science and Engineering: B*, 2002, **88**, 139–142.

143 D. C. Bobela, L. Gedvilas, M. Woodhouse, K. A. W. Horowitz and P. A. Basore, *Progress in Photovoltaics: Research and Applications*, 2017, **25**, 41–48.

144 T. Zhang and W. Lin, *Chem Soc Rev*, 2014, **43**, 5982–5993.

145 J. Willkomm, K. L. Orchard, A. Reynal, E. Pastor, J. R. Durrant and E. Reisner, *Chem Soc Rev*, 2016, **45**, 9–23.

146 W. Hou and S. B. Cronin, *Adv Funct Mater*, 2013, **23**, 1612–1619.

147 S. Wu, L. Wen, G. Cheng, R. Zheng and X. Wu, *ACS Appl Mater Interfaces*, 2013, **5**, 4769–4776.

148 B. Lamm, L. Zhou, P. Rao and M. Stefik, *ChemSusChem*, 2019, **12**, 1916–1924.

149 E. Yablonovitch, D. L. Allara, C. C. Chang, T. Gmitter and T. B. Bright, *Phys Rev Lett*, 1986, **57**, 249–252.

150 S. A. Martell, U. Werner-Zwanziger and M. Dasog, *Faraday Discuss*, 2020, **222**, 176–189.

151 F. E. Osterloh, *Chem Soc Rev*, 2013, **42**, 2294–2320.

152 R. Rossetti, J. L. Ellison, J. M. Gibson and L. E. Brus, *J Chem Phys*, 1984, **80**, 4464–4469.

153 D. Tanaka, Y. Oaki and H. Imai, *Chemical Communications*, 2010, **46**, 5286–5288.

154 J. C. Nie, J. Y. Yang, Y. Piao, H. Li, Y. Sun, Q. M. Xue, C. M. Xiong, R. F. Dou and Q. Y. Tu, *Appl Phys Lett*, 2008, **93**, 173104.

155 F. L. Souza, K. P. Lopes, E. Longo and E. R. Leite, *Physical Chemistry Chemical Physics*, 2009, **11**, 1215–1219.

156 I. Cesar, K. Sivula, A. Kay, R. Zboril and M. Grätzel, *The Journal of Physical Chemistry C*, 2009, **113**, 772–782.

157 T. Hisatomi, H. Dotan, M. Stefik, K. Sivula, A. Rothschild, M. Grätzel and N. Mathews, *Advanced Materials*, 2012, **24**, 2699–2702.

158 S. B. Zhang, S.-H. Wei and A. Zunger, *J Appl Phys*, 1998, **83**, 3192–3196.

159 J. Low, J. Yu, M. Jaroniec, S. Wageh and A. A. Al-Ghamdi, *Advanced Materials*, 2017, **29**, 1601694.

160 L. Zhang and M. Jaroniec, *Appl Surf Sci*, 2018, **430**, 2–17.

161 S. J. A. Moniz, S. A. Shevlin, D. J. Martin, Z.-X. Guo and J. Tang, *Energy Environ Sci*, 2015, **8**, 731–759.

162 R. Marschall, *Adv Funct Mater*, 2014, **24**, 2421–2440.

163 L. Zhang, G. Tan, S. Wei, H. Ren, A. Xia and Y. Luo, *Ceram Int*, 2013, **39**, 8597–8604.

164 K. Vinodgopal and P. v Kamat, *Environ Sci Technol*, 1995, **29**, 841–845.

165 S. J. Hong, S. Lee, J. S. Jang and J. S. Lee, *Energy Environ Sci*, 2011, **4**, 1781–1787.

166 Q. Xu, L. Zhang, B. Cheng, J. Fan and J. Yu, *Chem*, 2020, **6**, 1543–1559.

167 A. J. Bard, *Journal of Photochemistry*, 1979, **10**, 59–75.

168 M. Tabata, K. Maeda, M. Higashi, D. Lu, T. Takata, R. Abe and K. Domen, *Langmuir*, 2010, **26**, 9161–9165.

169 H. Tada, T. Mitsui, T. Kiyonaga, T. Akita and K. Tanaka, *Nat Mater*, 2006, **5**, 782–786.

170 X. Wang, G. Liu, Z.-G. Chen, F. Li, L. Wang, G. Q. Lu and H.-M. Cheng, *Chemical Communications*, 2009, 3452–3454.

171 J. Yu, S. Wang, J. Low and W. Xiao, *Physical Chemistry Chemical Physics*, 2013, **15**, 16883–16890.

172 C. Kim, K. M. Cho, A. Al-Saggaf, I. Gereige and H.-T. Jung, *ACS Catal*, 2018, **8**, 4170–4177.

173 Y.-S. Hu, A. Kleiman-Shwarsctein, A. J. Forman, D. Hazen, J.-N. Park and E. W. McFarland, *Chemistry of Materials*, 2008, **20**, 3803–3805.

174 D. W. Hwang, H. G. Kim, J. S. Lee, J. Kim, W. Li and S. H. Oh, *J Phys Chem B*, 2005, **109**, 2093–2102.

175 H. Kato and A. Kudo, *J Phys Chem B*, 2002, **106**, 5029–5034.

176 T. Ikeda, T. Nomoto, K. Eda, Y. Mizutani, H. Kato, A. Kudo and H. Onishi, *The Journal of Physical Chemistry C*, 2008, **112**, 1167–1173.

177 R. Asahi, T. Morikawa, T. Ohwaki, K. Aoki and Y. Taga, *Science (1979)*, 2001, **293**, 269–271.

178 G. R. Torres, T. Lindgren, J. Lu, C.-G. Granqvist and S.-E. Lindquist, *J Phys Chem B*, 2004, **108**, 5995–6003.

179 W. Choi, A. Termin and M. R. Hoffmann, *J Phys Chem*, 1994, **98**, 13669–13679.

180 R. Konta, T. Ishii, H. Kato and A. Kudo, *Journal of Physical Chemistry B*, 2004, **108**, 8992–8995.

181 M. Maruyama, A. Iwase, H. Kato, A. Kudo and H. Onishi, *The Journal of Physical Chemistry C*, 2009, **113**, 13918–13923.

182 F. F. Abdi, L. Han, A. H. M. Smets, M. Zeman, B. Dam and R. van de Krol, *Nat Commun*, 2013, **4**, 2195.

183 B. Pattengale, J. Ludwig and J. Huang, *The Journal of Physical Chemistry C*, 2016, **120**, 1421–1427.

184 W. Zhang, F. Wu, J. Li, D. Yan, J. Tao, Y. Ping and M. Liu, *ACS Energy Lett*, 2018, **3**, 2232–2239.

185 W. Luo, J. Wang, X. Zhao, Z. Zhao, Z. Li and Z. Zou, *Physical Chemistry Chemical Physics*, 2013, **15**, 1006–1013.

186 G. V. Govindaraju, J. M. Morbec, G. A. Galli and K.-S. Choi, *The Journal of Physical Chemistry C*, 2018, **122**, 19416–19424.

187 T. W. Kim, Y. Ping, G. A. Galli and K.-S. Choi, *Nat Commun*, 2015, **6**, 8769.

188 S. P. Berglund, D. W. Flaherty, N. T. Hahn, A. J. Bard and C. B. Mullins, *The Journal of Physical Chemistry C*, 2011, **115**, 3794–3802.

189 H. Li, P. Wen, A. Hoxie, C. Dun, S. Adhikari, Q. Li, C. Lu, D. S. Itanze, L. Jiang, D. Carroll, A. Lachgar, Y. Qiu and S. M. Geyer, *ACS Appl Mater Interfaces*, 2018, **10**, 17129–17139.

190 P. Dai, J. Xie, M. T. Mayer, X. Yang, J. Zhan and D. Wang, *Angewandte Chemie International Edition*, 2013, **52**, 11119–11123.

191 P. D. Tran, S. S. Pramana, V. S. Kale, M. Nguyen, S. Y. Chiam, S. K. Batabyal, L. H. Wong, J. Barber and J. Loo, *Chemistry – A European Journal*, 2012, **18**, 13994–13999.

192 F. Chen, Q. Zhu, Y. Wang, W. Cui, X. Su and Y. Li, *ACS Appl Mater Interfaces*, 2016, **8**, 31025–31031.

193 X.-Q. Bao, M. Fatima Cerqueira, P. Alpuim and L. Liu, *Chemical Communications*, 2015, **51**, 10742–10745.

194 S. D. Tilley, M. Cornuz, K. Sivula and M. Grätzel, *Angewandte Chemie International Edition*, 2010, **49**, 6405–6408.

195 M. W. Kanan and D. G. Nocera, *Science (1979)*, 2008, **321**, 1072–1075.

196 D. K. Zhong, J. Sun, H. Inumaru and D. R. Gamelin, *J Am Chem Soc*, 2009, **131**, 6086–6087.

197 M. Risch, V. Khare, I. Zaharieva, L. Gerencser, P. Chernev and H. Dau, *J Am Chem Soc*, 2009, **131**, 6936–6937.

198 J. Barber, *Inorg Chem*, 2008, **47**, 1700–1710.

199 T. W. Kim and K.-S. Choi, *Science (1979)*, 2014, **343**, 990–994.

200 J. F. de Brito, P. G. Corradini, M. V. B. Zanoni, F. Marken and L. H. Mascaro, *J Alloys Compd*, 2021, **851**, 156912.

201 F. le Formal, N. Tétreault, M. Cornuz, T. Moehl, M. Grätzel and K. Sivula, *Chem Sci*, 2011, **2**, 737–743.

202 J. Gao, L. Zhao, Y. Wang, G. Pan, Y. Wang and Y. LI, *Chem Phys*, 2020, **536**, 110791.

203 M. F. Gromboni, D. Coelho, L. H. Mascaro, A. Pockett and F. Marken, *Appl Catal B*, 2017, **200**, 133–140.

204 D. Eisenberg, H. S. Ahn and A. J. Bard, *J Am Chem Soc*, 2014, **136**, 14011–14014.

205 C. U. Maier, M. Specht and G. Bilger, *Int J Hydrogen Energy*, 1996, **21**, 859–864.

206 M. J. Kenney, M. Gong, Y. Li, J. Z. Wu, J. Feng, M. Lanza and H. Dai, *Science (1979)*, 2013, **342**, 836–840.

207 B. Mei, A. A. Permyakova, R. Frydendal, D. Bae, T. Pedersen, P. Malacrida, O. Hansen, I. E. L. Stephens, P. C. K. Vesborg, B. Seger and I. Chorkendorff, *J Phys Chem Lett*, 2014, **5**, 3456–3461.

208 S. Hu, M. R. Shaner, J. A. Beardslee, M. Lichterman, B. S. Brunschwig and N. S. Lewis, *Science (1979)*, 2014, **344**, 1005 LP – 1009.

209 D. v Esposito, I. Levin, T. P. Moffat and A. A. Talin, *Nat Mater*, 2013, **12**, 562–568.

210 Y. W. Chen, J. D. Prange, S. Dühnen, Y. Park, M. Gunji, C. E. D. Chidsey and P. C. McIntyre, *Nat Mater*, 2011, **10**, 539–544.

211 P. A. Kohl, S. N. Frank and A. J. Bard, *J Electrochem Soc*, 1977, **124**, 225–229.

212 B. Mei, T. Pedersen, P. Malacrida, D. Bae, R. Frydendal, O. Hansen, P. C. K. Vesborg, B. Seger and I. Chorkendorff, *The Journal of Physical Chemistry C*, 2015, **119**, 15019–15027.

213 L. Steier, J. Luo, M. Schreier, M. T. Mayer, T. Sajavaara and M. Grätzel, *ACS Nano*, 2015, **9**, 11775–11783.

214 T. Yao, R. Chen, J. Li, J. Han, W. Qin, H. Wang, J. Shi, F. Fan and C. Li, *J Am Chem Soc*, 2016, **138**, 13664–13672.

215 L. Rovelli, S. D. Tilley and K. Sivula, *ACS Appl Mater Interfaces*, 2013, **5**, 8018–8024.

216 J. Xia, N. Masaki, K. Jiang and S. Yanagida, *The Journal of Physical Chemistry C*, 2007, **111**, 8092–8097.

217 T. Hatanpää, M. Vehkamäki, M. Ritala and M. Leskelä, *Dalton Transactions*, 2010, **39**, 3219–3226.

218 P. Jalkanen, V. Tuboltsev, B. Marchand, A. Savin, M. Puttaswamy, M. Vehkamäki, K. Mizohata, M. Kemell, T. Hatanpää, V. Rogozin, J. Räisänen, M. Ritala and M. Leskelä, *J Phys Chem Lett*, 2014, **5**, 4319–4323.

219 B. Marchand, P. Jalkanen, V. Tuboltsev, M. Vehkamäki, M. Puttaswamy, M. Kemell, K. Mizohata, T. Hatanpää, A. Savin, J. Räisänen, M. Ritala and M. Leskelä, *The Journal of Physical Chemistry C*, 2016, **120**, 7313–7322.

220 M. Puttaswamy, M. Vehkamäki, K. Kukli, M. C. Dimri, M. Kemell, T. Hatanpää, M. J. Heikkilä, K. Mizohata, R. Stern, M. Ritala and M. Leskelä, *Thin Solid Films*, 2016, **611**, 78–87.

221 A. R. Akbashev, M. Falmbigl, A. v Plokhikh and J. E. Spanier, *CrystEngComm*, 2017, **19**, 166–170.

222 A. v Plokhikh, M. Falmbigl, I. S. Golovina, A. R. Akbashev, I. A. Karateev, M. Y. Presnyakov, A. L. Vasiliev and J. E. Spanier, *ChemPhysChem*, 2017, **18**, 1966–1970.

223 M. Vehkamäki, T. Hatanpää, M. Ritala and M. Leskelä, *J Mater Chem*, 2004, **14**, 3191–3197.

224 Q. Qiao, Y. W. Li, J. Z. Zhang, Z. G. Hu and J. H. Chu, *Thin Solid Films*, 2017, **622**, 65–70.

225 H. F. Liu, K. K. A. Antwi, Y. D. Wang, L. T. Ong, S. J. Chua and D. Z. Chi, *RSC Adv*, 2014, **4**, 58724–58731.

226 F. Zhang, G. Sun, W. Zhao, L. Wang, L. Zheng, S. Liu, B. Liu, L. Dong, X. Liu, G. Yan, L. Tian and Y. Zeng, *Journal of Physical Chemistry C*, 2013, **117**, 24579–24585.

227 J. Li, N. Mao, X. Li, F. Chen, Y. Li, K. Jiang, Z. Hu and J. Chu, *Solar Energy Materials and Solar Cells*, , DOI:10.1016/j.solmat.2019.110218.

228 B. Weng, F. Xu and J. Xu, *Nanotechnology*, , DOI:10.1088/0957-4484/25/45/455402.

229 M. J. Müller, K. Komander, C. Höhn, R. van de Krol and A. C. Bronneberg, *ACS Appl Nano Mater*, 2019, **2**, 6277–6286.

230 Q. Qiao, L. P. Jin, Y. W. Li, M. J. Li, Z. G. Hu and J. H. Chu, *AIP Adv*, , DOI:10.1063/1.4982728.

231 Y. D. Shen, Y. W. Li, W. M. Li, J. Z. Zhang, Z. G. Hu and J. H. Chu, *The Journal of Physical Chemistry C*, 2012, **116**, 3449–3456.

232 K. Kukli, M. Mikkor, A. Šutka, M. Kull, H. Seemen, J. Link, R. Stern and A. Tamm, *J Magn Magn Mater*, , DOI:10.1016/j.jmmm.2019.166167.

233 J. Harjuoja, T. Hatanpää, M. Vehkamäki, S. Väyrynen, M. Putkonen, L. Niinistö, M. Ritala, M. Leskelä and E. Rauhala, *Chemical Vapor Deposition*, 2005, **11**, 362–367.

234 X. Wang, Z. Guo, Y. Gao and J. Wang, *J Mater Res*, 2017, **32**, 37–44.

235 S. Chu, R. Zhao, R. Liu, Y. Gao, X. Wang, C. Liu, J. Chen and H. Zhou, *Semicond Sci Technol*, , DOI:10.1088/1361-6641/aae071.

236 Y. Gao, Y. Shao, L. Yan, H. Li, Y. Su, H. Meng and X. Wang, *Adv Funct Mater*, 2016, **26**, 4456–4463.

237 G. Y. Song, C. Oh, S. Sinha, J. Son and J. Heo, *ACS Appl Mater Interfaces*, 2017, **9**, 23909–23917.

238 F. Mattelaer, K. Geryl, G. Rampelberg, T. Dobbelaere, J. Dendooven and C. Detavernier, *RSC Adv*, 2016, **6**, 114658–114665.

239 G. Rampelberg, M. Schaekers, K. Martens, Q. Xie, D. Deduytsche, B. de Schutter, N. Blasco, J. Kittl and C. Detavernier, *Appl Phys Lett*, 2011, **98**, 162902.

240 T. Blanquart, J. Niinistö, M. Gavagnin, V. Longo, M. Heikkilä, E. Puukilainen, V. R. Pallem, C. Dussarrat, M. Ritala and M. Leskelä, *RSC Adv*, 2013, **3**, 1179–1185.

241 M. S. Weimer, I. S. Kim, P. Guo, R. D. Schaller, A. B. F. Martinson and A. S. Hock, *Chemistry of Materials*, 2017, **29**, 6238–6244.

242 W.-J. Lee and Y.-H. Chang, *Coatings*, , DOI:10.3390/coatings8120431.

243 M. B. Sreedhara, J. Ghatak, B. Bharath and C. N. R. Rao, *ACS Appl Mater Interfaces*, 2017, **9**, 3178–3185.

244 E. Østreng, K. B. Gandrud, Y. Hu, O. Nilsen and H. Fjellvåg, *J Mater Chem A Mater*, 2014, **2**, 15044–15051.

245 X. Chen, E. Pomerantseva, K. Gregorczyk, R. Ghodssi and G. Rubloff, *RSC Adv*, 2013, **3**, 4294–4302.

246 J. S. Daubert, N. P. Lewis, H. N. Gotsch, J. Z. Mundy, D. N. Monroe, E. C. Dickey, M. D. Losego and G. N. Parsons, *Chemistry of Materials*, 2015, **27**, 6524–6534.

247 Y. Lu, T. Zhu, W. van den Bergh, M. Stefik and K. Huang, *Angewandte Chemie - International Edition*, 2020, **59**, 17004–17011.

248 N. Muralidharan, C. N. Brock, A. P. Cohn, D. Schauben, R. E. Carter, L. Oakes, D. G. Walker and C. L. Pint, *ACS Nano*, 2017, **11**, 6243–6251.

249 V. P. Prasadam, B. Dey, S. Bulou, T. Schenk and N. Bahlawane, *Mater Today Chem*, 2019, **12**, 332–342.

250 G. Y. Song, C. Oh, S. Sinha, J. Son and J. Heo, *ACS Appl Mater Interfaces*, 2017, **9**, 23909–23917.

251 X. Yang, H. Xu, W. Liu, Q. Bi, L. Xu, J. Kang, M. N. Hedhili, B. Sun, X. Zhang and S. de Wolf, *Adv Electron Mater*, , DOI:10.1002/aelm.202000467.

252 H. Zhao, H. Gao, B. Li, Z. Song, T. Hu and F. Liu, *Mater Lett*, 2019, **252**, 215–218.

253 X. Chen, E. Pomerantseva, P. Banerjee, K. Gregorczyk, R. Ghodssi and G. Rubloff, *Chemistry of Materials*, 2012, **24**, 1255–1261.

254 H. Jung, K. Gerasopoulos, A. A. Talin and R. Ghodssi, *J Power Sources*, 2017, **340**, 89–97.

255 S.-D. Lee, Y.-J. Lee, J.-J. Rha, W. I. Park, S.-H. Kwon and J.-D. Kwon, *Current Applied Physics*, 2016, **16**, 245–250.

256 S. Boukhalfa, K. Evanoff and G. Yushin, *Energy Environ Sci*, 2012, **5**, 6872–6879.

257 F. Cerbu, H.-S. Chou, I. P. Radu, K. Martens, A. P. Peter, V. v Afanas’ev and A. Stesmans, *Physica Status Solidi (C) Current Topics in Solid State Physics*, 2015, **12**, 238–241.

258 V. P. Prasadam, N. Bahlawane, F. Mattelaer, G. Rampelberg, C. Detavernier, L. Fang, Y. Jiang, K. Martens, I. P. Parkin and I. Papakonstantinou, *Mater Today Chem*, 2019, **12**, 396–423.

259 M. Schuisky, K. Kukli, M. Ritala, A. Hårsta and M. Leskelä, *Chemical Vapor Deposition*, 2000, **6**, 139–145.

260 R. Waldo, in *Microbeam Anal.*, ed. R. A. Waldo, 1988, pp. 310–314.

261 J. Rumble, in *CRC Handbook of Chemistry and Physics*, CRC Press/Taylor & Francis, Boca Raton, FL, 102nd Edit., 2021.

262 R. Matero, A. Rahtu, M. Ritala, M. Leskelä and T. Sajavaara, *Thin Solid Films*, 2000, **368**, 1–7.

263 J. D. S. Newman and G. J. Blanchard, *Langmuir*, 2006, **22**, 5882–5887.

264 M. Rusek, T. Komossa, G. Bendt and S. Schulz, *J Cryst Growth*, 2017, **470**, 128–134.

265 F. Korkmaz, S. Cetinkaya and S. Eroglu, *Metallurgical and Materials Transactions B*, 2016, **47**, 2378–2385.

266 L. Leontie, M. Caraman, M. Alexe and C. Harnagea, *Surf Sci*, 2002, **507–510**, 480–485.

267 S. Tokunaga, H. Kato and A. Kudo, *Chemistry of Materials*, 2001, **13**, 4624–4628.

268 J. D. Bierlein and A. W. Sleight, *Solid State Commun*, 1975, **16**, 69–70.

269 P. Makuła, M. Pacia and W. Macyk, *J Phys Chem Lett*, 2018, **9**, 6814–6817.

270 A. Mills and S. le Hunte, *J Photochem Photobiol A Chem*, 1997, **108**, 1–35.

271 D. Bae, B. Seger, P. C. K. Vesborg, O. Hansen and I. Chorkendorff, *Chem Soc Rev*, 2017, **46**, 1933–1954.